MEIER, STEPHEN R., Ph.D. The Investigation of Variable Nernst Equilibria on Isolated Neurons and Coupled Neurons Forming Discrete and Continuous Networks. (2016)
Directed by Dr. Joseph Starobin. 97 pp.

Since the introduction of the Hodgkin-Huxley equations, used to describe the excitation of neurons, the Nernst equilibria for individual ion channels have assumed to be constant in time. Recent biological recordings call into question the validity of this assumption. Very little theoretical work has been done to address the issue of accounting for these non-static Nernst equilibria using the Hodgkin-Huxley formalism. This body of work incorporates non-static Nernst equilibria into the generalized Hodgkin-Huxley formalism by considering the first-order effects of the Nernst equation. It is further demonstrated that these effects are likely dominate in neurons with diameters much smaller than that of the squid giant axon and permeate important information processing regions of the brain such as the hippocampus. Particular results of interest include single-cell bursting due to the interplay of spatially separated neurons, pattern formation via spiral waves within a soliton-like regime, and quantifiable shifts in the multifractality of hippocampal neurons under the administration of various drugs at varying dosages. This work provides a new perspective on the variability of Nernst equilibria and demonstrates its utility in areas such as pharmacology and information processing.

THE INVESTIGATION OF VARIABLE NERNST EQUILIBRIA ON ISOLATED NEURONS AND COUPLED NEURONS FORMING DISCRETE AND CONTINUOUS NETWORKS

by

Stephen R. Meier

A Dissertation Submitted to
the Faculty of The Graduate School at
The University of North Carolina at Greensboro
in Partial Fulfillment
of the Requirements for the Degree
Doctor of Philosophy

Greensboro
2016

Approved by

_____
Committee Chair

APPROVAL PAGE

This dissertation written by Stephen R. Meier has been approved by the following committee of the Faculty of The Graduate School at The University of North Carolina at Greensboro.

Committee Chair _____
Joseph Starobin

Committee Members _____
Maya Chhetri

_____
Dennis LaJeunesse

_____
Jianjun Wei

_____
Daniel Herr

_____
Date of Acceptance by Committee

_____
Date of Final Oral Examination

TABLE OF CONTENTS

LIST OF TABLES

Page

LIST OF FIGURES

Page

CHAPTER I

INTRODUCTION

Much of the current neurocomputational literature, including research related to neural networks, has failed to accurately account for intrinsic feedback mechanisms working to counteract charge depletion within the smaller diameter neurons. Such neurons are prevalent across regions of the brain that are responsible for the processing of information and the conversion of short-term memory to long-term memory. More recent studies have attempted to better incorporate these feedback mechanisms within theoretical models of neural activity [CUZ+09, UJBS09, DZ11, BC11, For13], however no effort has been made to include these mechanisms in a continuous network of neural activity or to generalize these mechanisms to non ion specific conductive-based models.

Single-cell models which do try and account for these mechanisms are useful only for one or two particular types of neurons; for which modeling requires intimate knowledge of the ionic channels embedded within the cellular membrane. More physiologically accurate techniques require additional time-dependent equations and eat up valuable computation time. Before investigating the role that these mechanisms play in continuous networks, an effective description is needed as an alternative to the current leading procedures and techniques. One such reduction, presented in Chp. II, allows for computationally efficient neurosynaptic networks to be modeled while incorporating these mechanisms.

For single-cell models, the general electrical dynamics are well understood through phase-plane analysis. However for network models a similar approach does not yet exist, making the identification of network bifurcation points difficult [NC13]. Observing the phase-plane dynamics in constituent cells may provide some temporal and spatial resolution for when and where the network bifurcations could occur. Bifurcation points provide parametric thresholds for when a network changes behavior. Network bifurcations within the brain could be pathological, such as the trigger for an epileptic seizure, or physiological, such as accessing memory or forming a thought. Investigating these network transitions would allow us to better understand how these processes take place in the brain, leading to the prevention of seizures or even diseases such as Alzheimer's.

This work addresses both discrete and continuous networks. In discrete networks synaptic coupling is modeled as a delayed external potential difference and the focal point of electrical activity is the cell's nucleus (soma). The potential difference is assumed uniform along the axon, and the propagation is assumed instantaneous [vVH01]. Therefore, the cell's nucleus is directly affected by the incoming synaptic currents. Continuous networks allow for neural media to be treated using reaction-diffusion theory and little difference is made between soma, dendrite, axon, and synapse. Instead the media is treated as a medium for signal propagation and variation along this medium are accounted for by functions of space and time. Continuous networks allow for the propagation which discrete networks assume to be instantaneous. Both approaches are valid depending on the problem domain and an effort has been made to account for both where possible.

The region of the brain believed to have a dominant impact on memory and spatial reasoning is the hippocampus. Electrical signals within the hippocampus travel along the trisynaptic pathway which terminates at the subiculum. The subiculum is the main output of the hippocampus and is believed to be responsible for switching on and off circuitry located elsewhere in the brain. The subiculum's ability to transition between single firing and network bursting is believed to be critical to its functionality [O'M05]. Network bursting is discussed in greater detail within Sec. 2.1 of Chp. II, and the pertinent anatomy of the hippocampus is provided in Sec. 3.1 of Chp. III.

The sections which follow for this chapter help to provide a sufficient theoretical background for understanding what is most relevant to this work. In Sec. 1.1 the physics of the phospholipid bilayer is presented and discussed. An introduction to these topics helps in making sense of the Hodgkin-Huxley equations for membrane excitation. Sec. 1.2 deals with the probability for an ionic channel to be open or closed. The net membrane dynamics relies heavily on the precise timing of the ion channel's gating dynamics. Sec. 1.3 introduces the Hodgkin-Huxley equations for the squid giant axon. A familiarity with these equations and there origin is necessary for deriving the first-order reduction in Chp. II, which is fundamental to this work as a whole. Sec. 1.4 provides a short introduction to phase-space and bifurcation analysis for single neurons. Such terminology presented within this section is critical to understanding the soliton-like regime which is discussed often throughout Chp. II and Chp. III.

1.1 Excitable Bilayers

Fig. 1 depicts the membrane of an excitable cell. A chain of excitable cells allows for electrical signals to propagate within our central and peripheral nervous system.

The membrane is made up of a phospholipid bilayer and voltage-gated ion channels. The ion channels are embedded within the lipid-bilayer and fluctuate between open and closed states. The state of the ion channel affects the channel's conductance and how easily ions flow across the membrane.

Ions may accumulate on the extra- or intracellular membrane surfaces, forming potential gradients across the membrane. Ion channels open and close to relieve stress caused by these concentration gradients. At rest, the potential difference across the cellular membrane, due to a particular ion's concentration gradient, is referred to as its Nernst potential. Each ion channel has a unique Nernst potential depending on the external and internal ion concentrations.

Ion channels are also very selective for one particular ion. In order for multiple ion species to transverse into and out of the intracellular space a unique ion channel is required for each species of ion. Ions may transverse the cell membrane either passively or actively. Ion channels provide passive transport via diffusion and move *with* the concentration gradient. Ion pumps provide active transport via Adenosine Triphosphate (ATP) and move *against* the concentration gradient.

Distinct from passive and active transport, ion channels may have passive or active conductances. An ion channel with a passive conductance is one where the channel is in a permanent open state and therefore has a constant conductance. On the other hand, active ion channels vary in conductance between measured maximum and minimum values. Varying conductance values for an active ion channel is the result of conformational changes in membrane proteins which are responsible for opening and closing the channel. Therefore, the change in conductance is proportional to the probability that a particular protein conformation is thermodynamically favored.

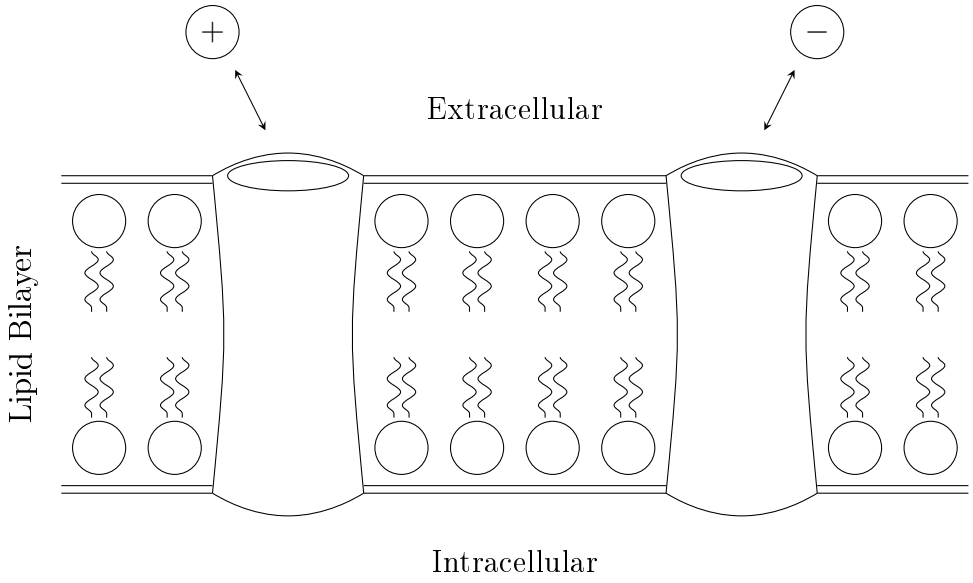

Figure 1. The Excitable Cell Membrane. The majority of neurons found in the brain are multipolar. Multipolar neurons consist of a cell body (soma), single axon, and many dendrites. Each component of the multipolar neuron has an excitable cell membrane. However, the ion channels embedded within these membranes vary from component to component which affects the propagation of signals long the neuron as a whole.

When thought of as an electrical component, the intracellular and extracellular membrane surfaces make up two sides of a parallel plate capacitor. The net charge which travels across the membrane, q, is then directly proportional to the potential difference across the cell membrane, V, (Eq. 1.1). Here the coefficient of proportionality is referred to as the membrane's capacitance, C.

$$q = CV. \tag{1.1}$$

The time variation of charge, $\dot{q}$, is equivalent to the net current due to all the ion channels, as well as any currents being applied to the membrane directly (Eq. 1.2).

Eq. 1.2 is a time-dependent equation for the trans-membrane potential difference, V, which is dependent upon the externally applied current, I_{app}, and the current of each ion channel, I_i, with the total number of ion channels being N.

$$C\frac{dV}{dt} = -\sum_{i=1}^{N} I_i + I_{\text{app}}. \tag{1.2}$$

By incorporating Ohm's law, $I_i = G_i(V - V_i)$, Eq. 1.2 is condensed to Eq. 1.3.

$$C\frac{dV}{dt} = -G_{\text{eff}}(V - V_{\text{eq}}) + I_{\text{app}}, \tag{1.3}$$

where the effective conductance G_{eff} and the equilibrium potential V_{eq} are given by

$$G_{\text{eff}} = \sum_{i=1}^{N} G_i, \tag{1.4}$$

$$V_{\text{eq}} = \frac{1}{G_{\text{eff}}}\sum_{i=1}^{N} G_i V_i, \tag{1.5}$$

with G_i being the channel conductance of the i^{th} ionic channel, and V_i being the Nernst potential for the i^{th} ionic channel.

1.2 Ion Channel Gating Dynamics

Active ion channels are ion channels with conductance values which vary in time. Active ion channels have a much richer range of dynamics then passive ion channels but this comes with a higher degree of complexity. Let's assume I_j, the jth ion channel

within our $\{1, 2, ..., N\}$ set of ion channels, has an active conductance characteristic. Then the ion channel may either be in an open state or a closed state. Let $P(n_{\mathrm{o}})$ be the probability that the ion channel is in an open state and let $P(n_{\mathrm{c}})$ be the probability that the ion channel is in a closed state. Also, let $P(n_{\mathrm{o}} \to n_{\mathrm{c}})$ be the probability that an ion channel in an open state will change to a closed state and $P(n_{\mathrm{c}} \to n_{\mathrm{o}})$ be the probability that an ion channel in a closed state will change to an open state.

Using the law of conditional probability, $P(n_{\mathrm{o}} \to n_{\mathrm{c}})P(n_{\mathrm{o}})$ represents the decrease in the probability of the channel being in an open state and $P(n_{\mathrm{c}} \to n_{\mathrm{o}})P(n_{\mathrm{c}})$ represents the decrease in the probability of the channel being in a closed state. The overall shift in the probability of an ion channel being in the open state, within an infinitesimal time, dt, is shown in Eq. 1.6.

$$\frac{d}{dt}P(n_{\mathrm{o}}) = \frac{d}{dt}\left[P(n_{\mathrm{c}} \to n_{\mathrm{o}})P(n_{\mathrm{c}}) - P(n_{\mathrm{o}} \to n_{\mathrm{c}})P(n_{\mathrm{o}})\right]. \tag{1.6}$$

Common throughout literature and this work, Eq. 1.6 is simplified to Eq. 1.7.

$$\frac{dn}{dt} = \alpha(1 - n) - \beta n, \tag{1.7}$$

where n is simply the probability of the ion channel to be in the open state, α is the rate of moving from a closed to open state, and β is the rate of moving from an open to closed state. Eq. 1.7 is referred to as a gating equation for the gating variable n. The typical number of gating variables is two, one for channel activation and another for channel inactivation. Channels with both activation and inactivation are referred to as *transient* while channels with only activation are referred to as

persistent. The forward and backward rates, α and β, in Eq. 1.7 are functions of the trans-membrane potential, V, and are experimentally fit to a Boltzmann distribution using the thermodynamic theory for ion channel activation.

1.3 The Hodgkin-Huxley Equations

In 1952 Alan Hodgkin and Andrew Huxley published a quantitative description of nerve excitation [HH52]. In 1963 they were awarded the *Nobel Prize in Physiology or Medicine* for their work. The Hodgkin-Huxley (HH) model includes three currents: an active-persistent potassium current, an active-transient sodium current, and a passive leakage current; represented by Eq. 1.8, Eq. 1.9, and Eq. 1.10 respectively.

$$I_{\mathrm{K}} = \bar{g}_{\mathrm{K}} n^4 \left(V - V_{\mathrm{K}}\right), \tag{1.8}$$

$$I_{\mathrm{Na}} = \bar{g}_{\mathrm{Na}} m^3 h \left(V - V_{\mathrm{Na}}\right), \tag{1.9}$$

$$I_{\mathrm{L}} = \bar{g}_{\mathrm{L}} \left(V - V_{\mathrm{L}}\right), \tag{1.10}$$

The gating variables (n, m, and h) from Eq. 1.8 and Eq. 1.9 have their own time-dependent equations, namely Eq. 1.11, Eq. 1.12, and Eq. 1.13.

$$\dot{n} = \alpha_n(V)(1-n) - \beta_n(V)n, \tag{1.11}$$

$$\dot{m} = \alpha_m(V)(1-m) - \beta_m(V)m, \tag{1.12}$$

$$\dot{h} = \alpha_h(V)(1-h) - \beta_h(V)h, \tag{1.13}$$

The rate equations for each of the gating variables are given by Eq. 1.14 - Eq. 1.19; where the trans-membrane potential, V, is given in millivolts.

$$\alpha_n(V) = 0.01(10-V)/\left\{\exp\left((10-V)/10\right)-1\right\}, \quad (1.14)$$

$$\beta_n(V) = 0.125\exp\left(-V/80\right), \quad (1.15)$$

$$\alpha_m(V) = 0.1(25-V)/\left\{\exp\left((25-V)/10\right)-1\right\}, \quad (1.16)$$

$$\beta_m(V) = 4\exp\left(-V/18\right), \quad (1.17)$$

$$\alpha_h(V) = 0.07\exp\left(-V/20\right), \quad (1.18)$$

$$\beta_h(V) = 1/\left\{\exp\left((30-V)/10\right)+1\right\}. \quad (1.19)$$

These equations, along with Eq. 1.3 in Sec. 1.1 make up the Hodgkin-Huxley equations used to describe electrical activity in the squid giant axon. All constant parameter values are listed in table 1.

Table 1. Parameters for the Hodgkin-Huxley Equations. This table includes the membrane capacitance, Nernst potentials, and maximum channel conductance values. The values and units for each are given on the right-hand side.

Parameter	Value
C	1 μF/cm^2
V_{K}	-12 mV
V_{Na}	120 mV
V_{L}	10.6 mV
$\bar{g}_{\mathrm{K}}$	36 mS/cm^2
$\bar{g}_{\mathrm{Na}}$	120 mS/cm^2
$\bar{g}_{\mathrm{L}}$	0.3 mS/cm^2

Fig. 2 shows the single-cell dynamics for the HH equations when a depolarizing external current is applied briefly at the four millisecond mark. The external stimulation is shown in Fig. 2:A and is labeled *depolarization*. After this brief stimulation we can see the cell activate. The cell's activation period is characterized by an increase in

the m and n channel activation variables and a decrease in the h channel deactivation variable, Fig. 2:B. The activation region is shown in Fig. 2:A and is labeled as the *upstroke* of the action potential.

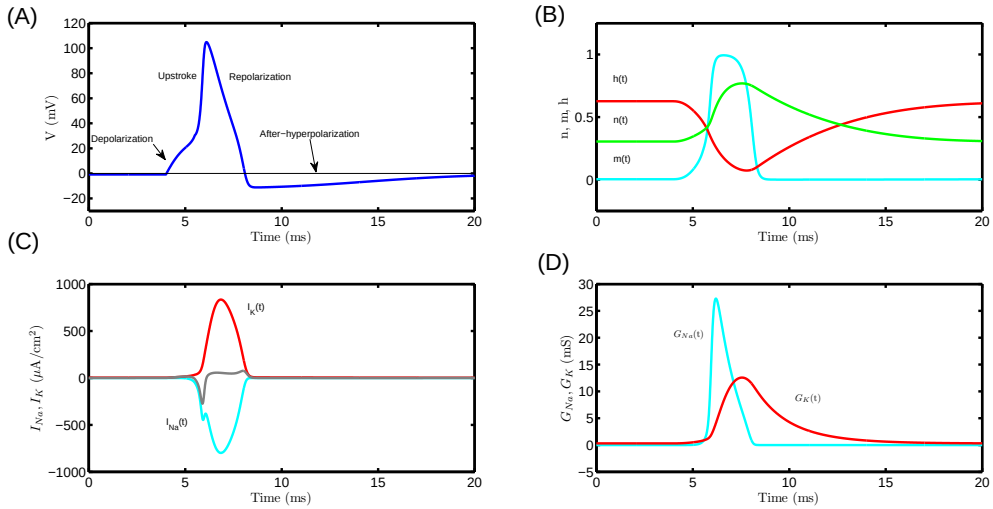

Figure 2. Hodgkin-Huxley Cell Excitation Event. A: Typical, single-cell, action potential with depolarization, upstroke, repolarization, and after-hyperpolarization regions indicated. B: Time dynamics of the potassium activation variable n, sodium activation variable m, and sodium in-activation variable h. C: Time dynamics of the inward sodium current (cyan), outward potassium current (red), and net ionic current (gray). D: Fast sodium conductance (cyan), and slower potassium conductance (red).

During cell activation, a fast jump in sodium conductivity can be observed, Fig. 2:D. This results in an inward sodium current, Fig. 2:C. This is followed by a much slower increase in potassium conductance, Fig. 2:D, and an outward potassium current which works to normalize the cellular membrane, Fig. 2:C. This outward potassium current works to deactivate the cellular membrane. This is shown in Fig. 2:A and is labeled as the *repolarization* of the action potential. Due to the slow nature of the outward potassium current there is also a region of time where

the membrane undershoots the equilibrium value. This is shown in Fig. 2:A and is labeled as the *after-hyperpolarization* of the membrane action potential.

Since its inception, the HH model has been extensively studied. Krinskii and Kokoz were able to reduce the HH model from four-equations to two-equations by assuming that sodium activates instantaneously (i.e. $m = m_\infty(V)$) and that the n and h gating variables are symmetric [KK73]. In 1961 Fitzhugh published his work on projecting the four dimensional HH phase-space to a two-dimensional phase-space [Fit61]. His work was pivotal to establishing the dynamical systems interpretation of modern computational neuroscience. In 1981 Catherine Morris and Harold Lecar employed the HH formalism when modeling barnacle muscle fiber [ML81]. Their work demonstrated the utility of symmetric α and β rates when modeling non-inactivating ion channels [LEL75]. In recent years phenomenological spiking models have been used to reduce the HH-like equations even further, an excellent review is given by Izhikevich [Izh04].

1.4 Phase-Space and Bifurcation Analysis

In this section the terminology for bifurcations in phase-space is presented with treatment given to the Andronov-Hopf bifurcation. The Andronov-Hopf bifurcation is the fundamental bifurcation which is explored in Chp. II and is responsible for single-cell bursting as a result of communication between spatially distant neurons. Many of the methods within this section are applied to the Morris-Lecar equations for cell excitation. Morris-Lecar is the same model which is used in Chp. II. However, these mathematical concepts and methods also apply to other dynamical systems with ease. The Morris-Lecar (ML) equations include an active-persistent calcium current, active-persistent potassium current, and a passive leakage current and was used to

model the barnacle giant muscle fiber [ML81]. The system of equations is shown in Eq. 1.20 - Eq. 1.21.

$$C\dot{V} = -G_{\text{eff}}(V,W)\left[V - V_{\text{eq}}(V,W)\right] + I_{\text{app}}, \tag{1.20}$$

$$\dot{W} = \left(W_{\infty}(V) - W\right)/\tau_{W}(V), \tag{1.21}$$

where the auxiliary equations are listed in Eq. 1.22 - Eq. 1.26 and the parameter values are in table 2.

$$G_{\text{eff}}(V,W) = \bar{g}_{\text{Ca}} M_{\infty}(V) + \bar{g}_{\text{K}} W + \bar{g}_{\text{L}}, \tag{1.22}$$

$$V_{\text{eq}}(V,W) = \left(\bar{g}_{\text{Ca}} M_{\infty}(V) V_{\text{ca}} + \bar{g}_{\text{K}} W V_{\text{K}} + \bar{g}_{\text{L}} V_{\text{L}}\right)/G_{\text{eff}}, \tag{1.23}$$

$$M_{\infty}(V) = \frac{1}{2}\left(1 + \tanh\left[\frac{V+1.2}{18}\right]\right), \tag{1.24}$$

$$W_{\infty}(V) = \frac{1}{2}\left(1 + \tanh\left[\frac{V-2}{30}\right]\right), \tag{1.25}$$

$$\tau_{W}(V) = \frac{1}{0.04}\text{sech}\left(\frac{V-2}{30}\right). \tag{1.26}$$

Fig. 3 shows a single excitation event using the ML model, this is similar to what was shown in Fig. 2 for the Hodgkin-Huxley model. In addition, a phase-space diagram for the action potential, presented in Fig. 3, is shown in Fig. 4.

The phase-space diagram is generated simply by plotting the two state variables (V and W) against one another. The green and red lines indicate the V and W nullclines, respectively. A *nullcline* is the trajectory in phase-space where the time derivative for the state variable is zero. The intersection of the V and W nullclines defines an equilibrium point for the dynamical system. When the system is at equilibrium neither state variable changes with respect to time, and therefore the cellular

membrane remains in a resting state where the net ionic current across the membrane is zero and the transmembrane potential equals the average Nernst potential.

Table 2. Parameters for the Morris-Lecar Equations. This table includes the membrane capacitance, Nernst potentials, and maximum channel conductance values. The values and units for each are given on the right-hand side.

Parameter	Value
C	20 μF/cm^2
V_{K}	-84 mV
V_{Ca}	130 mV
V_{L}	-60 mV
$\bar{g}_{\mathrm{K}}$	8 mS/cm^2
$\bar{g}_{\mathrm{Ca}}$	4.4 mS/cm^2
$\bar{g}_{\mathrm{L}}$	2 mS/cm^2

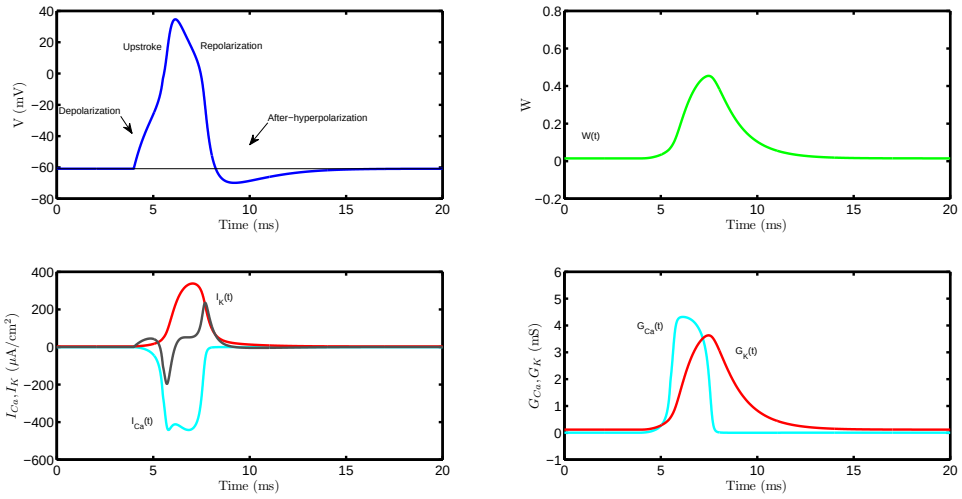

Figure 3. Morris-Lecar Cell Excitation Event. The indicators and coloring conventions are equivalent to those presented with Figure 2 for the Hodgkin-Huxley model.

Given any point in phase-space there exists a unique trajectory for the system to follow. The electrical potential profile in Fig. 3 is the result of following the circular

trajectory in Fig. 4. At any point in phase-space the direction is given by the vector $(\dot{V}, \dot{W})$. The collection of $(\dot{V}, \dot{W})$ vectors is known as a *direction field*. The direction field in phase-space is greatly influenced by the stability of equilibria, such as the one indicated in Fig. 3 where the nullclines intersect. When the stability of an equilibrium point changes, or the equilibrium point disappears, it affects the direction field and corresponding system trajectory.

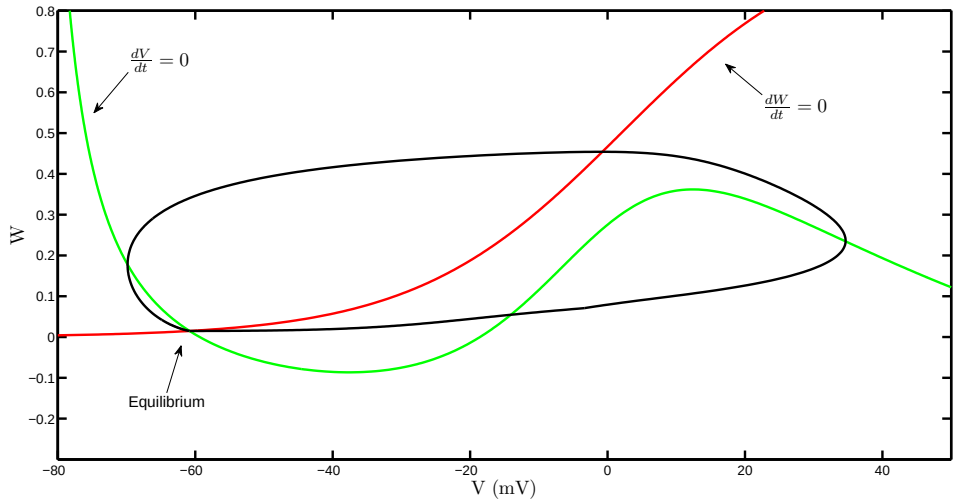

Figure 4. Phase-Space for the Morris-Lecar Model. This figure depicts one excitation event using the standard parameter set presented in Table 2.

When an equilibrium point disappears the direction field undergoes a transition know as a *Saddle-Node* bifurcation. Likewise, when an equilibrium point loses stability the direction field undergoes a transition known as an *Andronov-Hopf* bifurcation. The loss of stability is quantified by completely imaginary eigenvalues in the linear system localized to the equilibrium point. This local equivalency in the neighborhood of an equilibrium point is known as the Hartman-Grobman theorem [HI97].

Because of this local equivalency there exists a unique linear system for each equilibrium point in phase-space which is equivalent to the nonlinear system localize at that point. For ML, the non-linear system is given in Eq. 1.27 and Eq. 1.28, where $f(V,W)$ and $g(V,W)$ are set by solving Eq. 1.20 and Eq. 1.21 for $\dot{V}$ and $\dot{W}$.

$$\dot{V} = f(V,W) \tag{1.27}$$

$$\dot{W} = g(V,W). \tag{1.28}$$

The linear system for approximating the non-linear system of equations, Eq. 1.27 and Eq. 1.28, is given in matrix form in Eq. 1.29 and follows directly by performing a Taylor expansion around the equilibrium point (V_0, W_0).

$$\begin{pmatrix} \dot{V} \\ \dot{W} \end{pmatrix} \approx \begin{pmatrix} \frac{\partial f}{\partial V} & \frac{\partial f}{\partial W} \\ \frac{\partial g}{\partial V} & \frac{\partial g}{\partial W} \end{pmatrix} \begin{pmatrix} V - V_0 \\ W - W_0 \end{pmatrix}. \tag{1.29}$$

The eigenvalues for the equilibrium point in Fig. 4, (V_0, W_0), are $-0.082 \pm 0.016i$. If we apply a current density, I_{app}, of 95 μA/cm^2 to the cell membrane the system's nullclines shift and the eigenvalues of the equilibrium point change to $0.021 \pm 0.070i$.

The change in sign of the real-part of the eigenvalues indicates that there exists a value for I_{app} between 0 μA/cm^2 and 95 μA/cm^2 which will cause the eigenvalues of the equilibrium point to be purely imaginary. This point corresponds to the bifurcation point and the loss in stability for the equilibrium point. This occurs when $I_{\text{app}} = 88.559$ μA/cm^2.

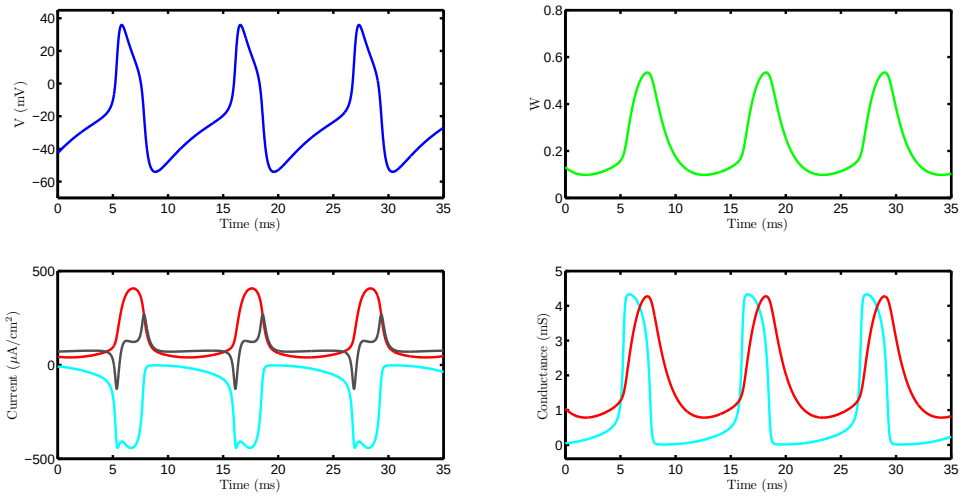

Figure 5. Morris-Lecar Bifurcation Event. Using the applied current as a bifurcation parameter the eigenvalues for the linearized system, localized to the bifurcation point (V_0, W_0), become purely imaginary when the equilibrium point loses stability. This figure demonstrates continuous excitation events following the loss in equilibrium stability.

The change to purely imaginary eigenvalues is indicative of an Andronov-Hopf bifurcation over the injected current parameter, I_{app}. The new cell behavior, when the equilibrium point is unstable, is depicted is Fig. 5. The continuous firing pattern of the cell in Fig. 5 is referred to as a *stable limit-cycle* in phase-space. In the vicinity of this bifurcation point an *unstable limit-cycle* also exists.

1.5 Summary and Outline

Many fundamental theoretical concepts and procedures have been presented in this chapter. In Sec. 1.1 the excitable cellular membrane was introduced along with a discussion on ionic channels. Ohm's law and Kirchhoff's current law are used to construct the fundamental framework upon which the Hodgkin-Huxley equations were built. In Sec. 1.2 the thermodynamics for the open and closed states of ion channels

was considered using the principle of detailed balance and time-dependent equations were derived which allow for the transitions between these states to be modeled. In Sec. 1.3 the Hodgkin-Huxley equations were introduced, building upon the topics discussed in the previous sections. In Sec. 1.4 the Morris-Lecar model is presented along with methods for identifying bifurcations points in phase-space.

Chapter. II builds heavily upon the topics introduced in this chapter. In Chapter. II the unstable limit-cycle for the Andronov-Hopf bifurcation discussed in Sec. 1.4 is employed within a continuous network of neurons to demonstrate single-cell bursting as a result of communication between spatially separated neurons. The bifurcation dynamics are detailed to a finer degree of accuracy and a derivation of the soliton-like regime for the Fitzhugh-Nagumo model is presented. The soliton-like regime is of particular interest due to the unique network dynamics taking place within the vicinity of an Andronov-Hopf bifurcation for the constituent cells making up the network. In Sec. 1.4 the bifurcation parameter was the applied current. However, in Chapter. II the bifurcation parameter will be the shift in the Nernst equilibria for the ionic channels making up the membrane. This is a critical conceptual shift and is a detail that should be established first and foremost when reading through Chapter. II.

CHAPTER II

BURSTING REGIMES IN A REACTION-DIFFUSION SYSTEM WITH ACTION POTENTIAL-DEPENDENT EQUILIBRIUM

Understanding neural activity is an endeavor spanning several decades of research. Promising advances have been made in modeling both individual neurons as well as the combination of neurons making up a network. The goal of such work is to understand how our brains store and access information through identifying the internal and external factors which play important roles in these processes. In particular, synchronization of the electrical disturbances in neurons, or action potentials, is believed to play a crucial role in memory formation [AMF$^+$06a].

By introducing additional nonlinearities to the governing equations, a strong tedency toward synchronization in one-dimensional cables was previously observed within the "soliton-like regime" of the Fitzhugh-Nagumo model [AM97]. Such examples of synchronization within simple two-variable systems are of great interest for studying memory formation, and in this paper we present a physiologically-motivated modification to a similar two-variable system: the Morris-Lecar model [ML81,LEL75], which represents a reduced system based on the Hodgkin-Huxley model [HH52], emperically obtained to describe the voltage dynamics in the squid giant axon.

Recently, Gonzalez-Perez and collaboroators [GPBM$^+$14] presented an experimental study on the behavior of action potential propagation within invertebrates in which it was shown that contrary some well-known predictions of the Hodgkin-Huxley model, it is possible for action potential pulses to "pass through" each other

instead of annihilating upon contact. This soliton-like behavior motivated the authors to abandon a description of their results in terms of Hodgkin-Huxley-like models and employ a model for action potentials in terms of soliton-like sound pulses [GPBM$^+$14]. The authors did concede, however, that certain results [AM97] suggest Hodgkin-Huxley-like models *could* support such soliton-like behavior with suitable modifications to parameters. The present work serves as a bridge between recent experimental studies [GPBM$^+$14] and well-known theoretical results involving these soliton-like regimes [AM99, AM97] by demonstrating how the soliton-like regime emerges within the Morris-Lecar model when leading-order effects due to small cell size are included.

While the Morris-Lecar model is used as a particular example, the main goal of this paper is to explore a technique for incorporating voltage-dependent Nernst potentials into Hodgkin-Huxley-like models. The observation that a variable Nernst potential affects ionic relaxation times has been stated previously by Cressman et al [CUZ$^+$09]. Due to the very small size of brain axons, the cellular Nernst equilibrium potential is expected change in response to considerable intracellular charge depletion [PB07]. Here, we wish to account for this effect in neurons with radii several orders of magnitude smaller than that of the squid giant axon. Within this size regime, intracellular charge depletion becomes significant. Accounting for intracellular charge depletion also helps to quantify variations in cell size due to cell swelling which has been observed during epileptic seizures [CUZ$^+$09].

The chapter is organized as follows: Section 2.1 provides context for the work, containing a brief overview of Hodgkin-Huxley-like, reaction-diffusion models, as well as a discussion of neuronal bursting and how our approach enables us to investigate

this phenomenon. A scheme for incorporating a voltage-dependent Nernst potential into models derivable from the Hodgkin-Huxley system is proposed in Section 2.2, and an explicit implementation in the Morris-Lecar model is presented with a discussion of some of the immediate consequences of this generalization. Detailed results from these investigations are reported in Section 2.3. Finally, the conclusions and discussion are contained in Section 2.5.

2.1 Background

Memory formation [AMF+06b] and memory retention have been linked to neural synchronization since the introduction of the "binding problem," [M.74] which concerns how the brain constructs effective equivalence classes of objects deemed "similar." Support for the link between memory and neural synchronization has strengthened over the years, but the exact spatio-temporal dynamics and phase-locking characteristics have yet to be realized are expected to be extremely complex. The system is quite delicate, as deviations from physiologically acceptable conditions can result in memory distortion or impairment [BW01]. Understanding how these networks can erode in time will help in developing proactive measures to prevent irreversible network damage.

When building successful models, it is imperative to understand the fundamental constituents in great detail. Regarding electrical activity in the brain, the basic building blocks are excitable cells. Hodgkin and Huxley [HH52] pioneered significant progress in this realm with the introduction of a semi-empirical set of differential equations describing the voltage dynamics in a squid giant axon. The essential ingredients for generating an action potential in a single, excitable cell are a fast inward ionic current followed by a slower outward ionic current. Additional physical currents

may also exist, but the key feature is a "lumping" of the dominant currents into "fast" and "slow" groups. This qualitative grouping of many different physical processes into two groups is the basis for many of the two-variable systems which were later introduced as qualitatively similar models [ML81,PR94,Fit61] whose technical simplicity allowed for sophisticated mathematical analysis.

There are many different techniques for extracting a short list of rules from the differential equations governing single neurons which can be applied to a neural network representation such as a cellular automata [GdADM10] or mean-field model [Tre93]. In retaining the full range of single-cell dynamics one must choose between a discrete network representation or a continuous network representation via reaction-diffusion theory. Reaction-diffusion systems provide a universal network structure upon which one may unambiguously investigate various neural coupling strengths via different diffusion profiles. Discrete networks provide a much wider array of possible network structures, and this may naturally result in structurally-dependent coupling profiles. However, it should be noted that, when discretized for numerical simulation, continuous reaction-diffusion systems are nothing more than special cases of discrete networks, and the distinction between the two becomes less apparent. In the present work, the focus will be in exploring the predictions of the continuum limit through numerical work involving a discrete representation of a continuous system.

Network instabilities and abnormalities are thought to be critical features in any detailed explanation of mental diseases such as epilepsy and Alzheimer's disease. Research into seizure activity [UJBS09] suggests that the slight variations of cellular resting potentials due to changes in ionic concentrations during excitation events have

observable consequences which are not predicted by conventional models employing static Nernst potentials.

2.1.1 Effects of Small Diameter Neurons

Conventional Hodgkin-Huxley like single cell models assume that the intracellular and extracellular ion concentrations act as charge reservoirs [HH52]. As a result, there is never a net loss or gain in ions across the membrane boundry and the Nernst potentials remain constant over the span of many excitation events.

To investigate this assumption let's begin with the following conservation law, Eq. 2.1 (adapted from Cressman *et. al* [CUZ$^+$09]).

$$\Delta c_i \mathrm{Vol}_i = -\Delta c_o \mathrm{Vol}_o. \tag{2.1}$$

Here Δc_i is the change in concentration of intracellular ions, Vol_i is the volume of intracellular space, Δc_o is the change in concentration of extracellular ions, and Vol_o is the volume of extracellular space.

"I" from the Hodgkin-Huxley equations is the current density across the membrane. Therefore, if A is the surface area of the membrane, $i_{tot} = IA$ is the total current flowing into the cell. After some Δt has elapsed the change to the amount of intracellular charge would be equal to $\Delta Q = i_{tot}\Delta t$. The number of ions entering the cell is then $\Delta N = \Delta Q/q$, where q is the elementry charge unit. The number concentration of ions is then $\Delta N/\mathrm{Vol}_i$. Which, when using Avogadro's number N_a, may be converted to the molar concentration $\Delta c_i = \Delta N/(N_a \mathrm{Vol}_i)$. The rate of change in the intracellular ion concentration is then equal to Eq. 2.2.

$$\frac{\Delta c_i}{\Delta t} = \left(\frac{I}{qN_a}\right)\frac{A}{\mathrm{Vol}_i}. \tag{2.2}$$

Eq. 2.2 shows why the original assumption that intracellular and extracellular space act as charge reservoirs was vaild for cells with small surface-to-volume ratios (i.e. $A/\mathrm{Vol}_i \to 0$). Although when considering small cell, like in the brain, the rate change in ion concentration should not be ignored.

During the process of an action potential, charges move across the cell membrane through ionic channels. If the fraction of total charge leaving the cell is substantial, the cell becomes significantly charge-depleted. For large-diameter axons this effect is minimal. However, for smaller neurons such as those in the neocortex, this effect may not be negligible. A substantial charge depletion would dramatically affect the resting potential of the ionic channels [PB07]. We quantify charge depletion δ as the ratio of surface charge to the amount of internal charge at some constant voltage. It is useful to define,

$$\begin{aligned} Q_s &= VC(\pi dL), & (2.3)\\ Q_i &= F[M]\left(\frac{\pi d^2 L}{4}\right), & (2.4)\\ \delta &= Q_s/Q_i = \beta(1/d), & (2.5) \end{aligned}$$

where V is the trans-membrane potential, Q_s is the amount of charge stored on the cell surface for a capacitance C (per unit area), Q_i is the amount of intracellular charge found for an ionic concentration density $[M]$, F is Faraday's constant, d is the cell's diameter, L is the length of the cell, and $\beta = (4VC)/(F[M])$. For simplicity, we consider a cylindrical axon.

The diameters of typical axons in the neocortex are roughly three orders of magnitude smaller than the diameter of the squid giant axon [KS09,DCB$^+$11]. Therefore, δ is not small and charge depletion cannot be neglected. To take this into consideration we propose a method for introducing dynamical shifts in Nernst potential which are functions of the instantaneous trans-membrane potential. While the cell membrane may contain many different ionic channels, we model the shift in the effective Nernst potential of the entire membrane.

2.1.2 Nernst Potential Shift

Conventional modeling of neuronal excitation takes place on many different levels of detail [Izh04], from the physiologically-detailed and mathematically cumbersome models [TWMM91, RGWB69] to the qualitatively accurate but mathematically transparent systems [PR94, Fit61, Izh04]. A popular class of models is based on the representation of the excitable cell as a circuit in which separate channels exist for each important group of charge-carrying ions. A few well-known examples are the Hodgkin-Huxley [HH52] and Morris-Lecar [ML81] models. The fundamental equation of any model representable as a circuit is conservation of charge, which may be written as a differential equation for membrane potential V as [KS09],

$$C\dot{V} = -G_{\text{eff}}(V - V_{\text{eq}}) + I_{\text{app}}, \tag{2.6}$$

where the effective conductance G_{eff} and the equilibrium membrane potential V_{eq} are given by

$$G_{\text{eff}} = \sum_{i=1}^{N} G_i, \tag{2.7}$$

$$V_{\text{eq}} = \frac{1}{G_{\text{eff}}} \sum_{i=1}^{N} G_i V_i, \tag{2.8}$$

with G_i being the channel conductance of the i^{th} ionic channel, N being the total number of ionic channels embedded within the cell membrane, and V_i being the Nernst potential for the ith ionic channel.

For passive channels G_i is a constant value, and the channel acts like a simple, Ohmic resistor. When the i^{th} ionic channel is active, G_i becomes a function of one or more gating-variables, each of which depends on the membrane potential. The quantity G_{eff} is the total conductance over all ionic channels, and V_{eq} is the average Nernst potential (weighted by channel conductance). In order for the Nernst potential of a particular ionic channel to remain constant, the intracellular and extracellular ion concentrations must not change by a significant amount over the course of an action potential ($\delta \ll 1$). On the contrary, for substantial charge depletion, δ becomes on the order of unity.

2.1.3 Conventional Morris-Lecar Model

This work incorporates the effects due to significant charge depletion into the two-variable Morris-Lecar model,

$$C\dot{V} = [-G_{\text{eff}}(V,W)(V - V_{\text{eq}}(V,W))] + I_{\text{app}}(t), \tag{2.9}$$

$$\dot{W} = (W_\infty(V) - W)/\tau_W(V), \tag{2.10}$$

originally obtained from the study of barnacle muscle fibers. Here, V is the instantaneous membrane potential as before, W is a dimensionless gating variable corresponding to the inhibitory response of the potassium channel, and $I_{\rm app}(t)$ is any applied, stimulation current. In this two-variable system, the calcium dynamics are assumed to act on such short timescales that the calcium channel instantaneously finds its voltage-dependent equilibrium state, so $M_\infty(V)$ has no intrinsic dynamics. The potassium dynamics are modeled through the evolution of the dynamical gating variable W. The explicit forms for the effective conductance, equilibrium potential and other voltage-dependent functions are

$$
\begin{aligned}
G_{\rm eff}(V,W) &= g_{Ca}M_\infty(V) + g_K W + g_L,, && (2.11)\\
V_{\rm eq}(V,W) &= (g_{Ca}M_\infty(V)V_{Ca} + g_K W V_K + g_L V_L)/G_{\rm eff}, && (2.12)\\
M_\infty(V) &= \frac{1}{2}\left(1+\tanh\left[\frac{V-V_1}{V_2}\right]\right), && (2.13)\\
W_\infty(V) &= \frac{1}{2}\left(1+\tanh\left[\frac{V-V_3}{V_4}\right]\right), && (2.14)\\
\tau_W(V) &= \frac{1}{\phi}{\rm sech}\left(\frac{V-V_3}{2V_4}\right). && (2.15)
\end{aligned}
$$

Typical values for the parameters are shown in Table. 3. Using these dimensions, voltage is measured in mV and time in ms. The sodium gating variable, which acts on very fast timescales is represented by the effective step-function, $M_\infty(V)$, and posesses no intrinsic dynamics in the two-variable model. A typical action potential due to a short stimulation current is shown in Fig. 6.

Table 3. Parameters for the Morris-Lecar Equations. These parameters were used for the simulations discussed throughout Chapter II and appear in Eqs. 2.9-2.10.

Parameter	Value
C	20 μF/cm^2
ϕ	0.04
g_{Ca}	4.4 μS/cm^2
g_K	8 μS/cm^2
g_L	2 μS/cm^2
V_{Ca}	130 mV
V_K	-84 mV
V_L	-60 mV
V_1	-1.2 mV
V_2	18 mV
V_3	2 mV
V_4	30 mV

2.1.4 Single-Cell Bursting

An action potential pulse train which is modulated by a slower applied current is referred to as a *bursting* event. Bursting allows for neurotransmitter concentrations to reach levels above that of simple action potential pulse trains [WLL$^+$12] and is a critical component to many cellular networks [NHCG98, LYL$^+$12].

Several types of bursting have been demonstrated in the Morris-Lecar model using Eq. 2.16 as a slow ($\epsilon \ll 1$) external current to modulate the signal's pulse train [DZ11].

$$\frac{dI_{\text{app}}}{dt} = \epsilon \left(V_0 - V\right). \tag{2.16}$$

Recent studies support both pathological [CUZ$^+$09] and physiological [For13] forms of bursting, as well as single-cell [For14] and network [RFT$^+$08] bursting.

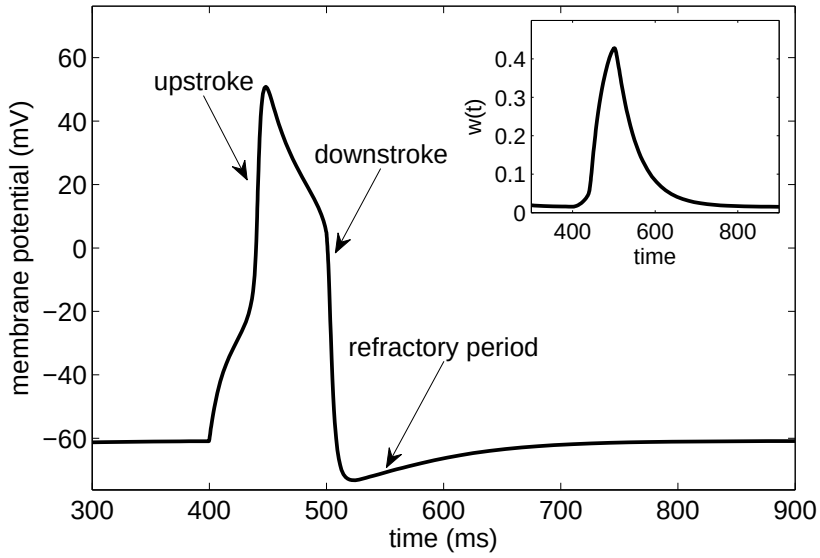

Figure 6. Action Potential Shape within the Morris Lecar Model. A stimulus is applied to the resting cell at $t = 400$ms. Corresponding behavior of recovery variable $W(t)$ is shown in the inset.

It is likely that the role bursting plays within a particular system is highly dependent on where that system is located in the brain. Even though experimentally recorded bursting can be easily related to autogenerative regimes in the big nerves, the mechanisms for bursting in the networks of small brain axons are not well understood.

2.1.5 Discrete and Continuous Networks

Neurons firing in isolation are unable to transmit vital signals within the brain. Network models allow for the electrical activity of one neuron to act as an external input for another neuron. This helps to model the transmission of electrical signals traveling around the brain. Neurons within the brain are *multipolar* in structure with multiple electrical inputs and outputs. Fig. 8 is a schematic of two connected multipolar neurons.

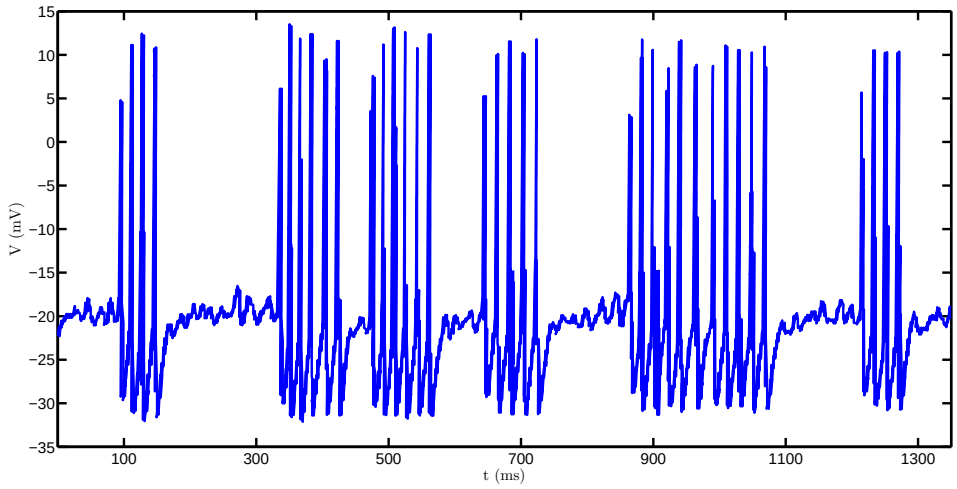

Figure 7. Bursting within the Rodent Brain. Experimental recorded bursting patterns for a single neuron within the rodent trigeminal nerve presented by Negro *et. al* [NHCG98].

The typical components of a neuron include the dendrites, the cell body (or soma), the axon, and the synapses. For multipolar neurons, these components are structured from left to right in Fig. 8.

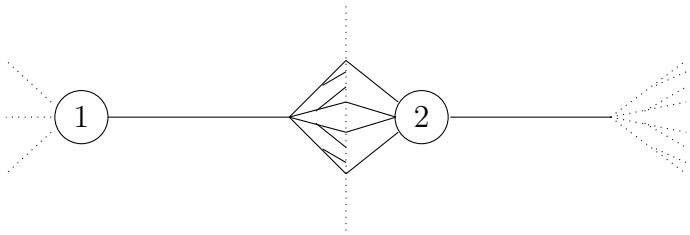

Figure 8. Two Connected Multipolar Neurons. Neurons in the brain are heavily branched and interconnected. In addition, the connections between neurons are subject to synaptic plasticity and may change over time due to long-term potentiation.

All four of these compartments are modeled using the Hodgkin-Huxley formalism. This was demonstrated in 1991 for the CA1/CA3 hippocampal neurons by Traub

et. al [TWMM91]. The number of HH-like equations needed to represent a single pyramidal neuron in the CA1/CA3 hippocampal region is nineteen.

It is quite difficult to perform phase-plane analysis on a nonlinear system this large. As a result, in 1994 Pinsky and Rinzel derived a reduced system of two equations, maintaining all the relevant phase-plane dynamics found in Traub's model [PR94]. This reduction is more applicable to exact phase-plane solutions and allows for network models which are more computationally efficient.

The biological connection between two neurons takes place within a region known as the synaptic cleft. The synapse of a presynaptic cell and the dendrite of a postsynaptic cell make up two ends of the cleft. Neurotransmitters originate at the presynaptic cell's synapse, locally diffuse through the media, and are collected by the postsynaptic cell's dendrite. These ions then work to excite the postsynaptic cell. If the excitation within the postsynaptic cell is large enough to elicit a propagating action potential the process repeats itself and the signal is transmitted. In the case of discrete networks, the synaptic input, Eq. 2.17, is added to the applied current, I_{app}, in Eq. 1.2.

$$I_{\text{syn}} = -\sum_{i}^{N} G_i(\Delta t)\,(V - V_i)\,. \tag{2.17}$$

Eq. 2.17 is similar to the current generated by an active ion channel but the conductance has a different functional dependence. The conductance for the synaptic current is dependent upon the amount of time which has elapsed since the last firing event of the presynaptic neuron, where the neurotransmitter originates. This ap-

proach assumes that the neurotransmitter diffuses across the synaptic cleft within a set amount of time. This is modeled this using Eq. 2.18.

$$G_i(\Delta t) = \bar{g}_i f(\Delta t). \tag{2.18}$$

The conductance is distributed over time based upon the diffusive rate of the neurotransmitter, Eq. 2.19.

$$f(\Delta t) = \frac{1}{\tau_1 - \tau_2} \left(e^{-\frac{\Delta t}{\tau_1}} - e^{-\frac{\Delta t}{\tau_2}} \right) \mathcal{H}(\Delta t). \tag{2.19}$$

In Eq. 2.19, $\mathcal{H}(\Delta t)$ is the Heaviside function and ensures that the conductance is zero if the presynaptic neuron has yet to fire. The peak and spread of the distribution, $f(\Delta t)$, dictates whether the presynaptic cell is less likely to elicit a firing event in the postsynaptic cell (i.e. an *inhibitory* neurotransmitter) or more likely to elicit a firing event in the postsynaptic cell (i.e. an *excitatory* neurotransmitter) [vVH01].

Discrete networks make the assumption that each cell is space-clamped. A space-clamped cell maintains a constant voltage value along its entire length. As a result, the cell's electrical signal travels from one end to the other instantaneously. A network of space-clamped cells is most useful when modeling localized network events due to the lack of propagating electrical signals.

Continuous networks, modeled via reaction-diffusion equations like Eq. 2.20, include the propagating effects of the electrical potential. This allows for nonlocalized network events to occur.

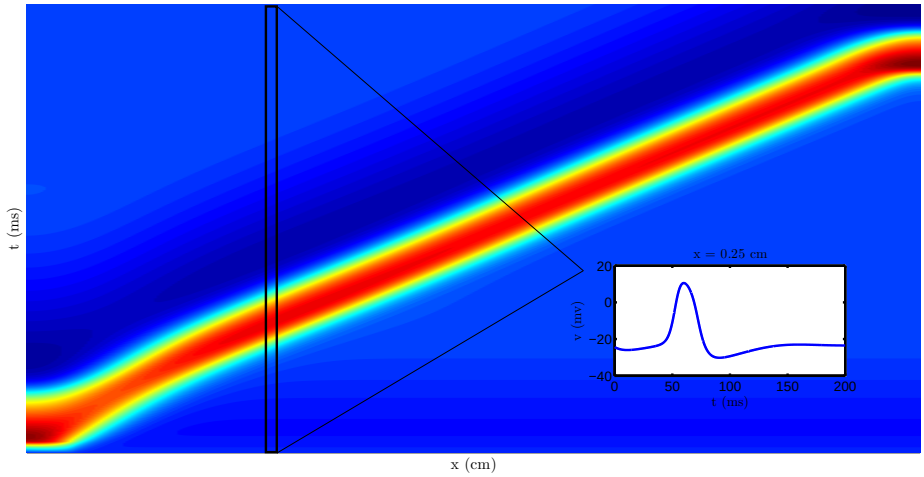

Figure 9. Propagating Action Potential using the ML System of Equations. This is a plot for a one-dimensional propagation action potential. The x-axis is the position long the cable and the y-axis is time. The color contrast for the plot is the transmembrane potential. Projected to one single spatial location give a plot of the transmembrane potential vs. time (see inlay).

A full derivation is provided by Keener [KS09] with a cellular neural network interpretation given by Slavova [Sla08].

$$C\frac{\partial V}{\partial t} = D\frac{\partial^2 V}{\partial x^2} - G_{\text{eff}}(V,W)\left[V - V_{\text{eq}}(V,W)\right] + I_{\text{app}}(x,t). \tag{2.20}$$

The diffusion coefficient, D, plays an analogous role to the neurotransmitter in the discrete networks. Fig. 9 shows a standard propagating action potential. A plot similar to Fig. 3 is generated by projecting to one point in space (see Fig. 9 inlay).

Solving Eq. 2.20 must be done numerically due to the nonlinearity of the equations. Some well-known options include explicit Runge-Kutta, and implicit Root Finding. Explicit Runge-Kutta provides high accuracy but isn't guaranteed to be stable. However, even when working in two spatial dimensions the explicit Runge-Kutta scheme

is quite robust. Implicit Root Finding provides a greater degree of stability but requires more time to achieve the same accuracy as the explicit Runge-Kutta scheme. In addition the Alternating Direction implicit method works very well for two spatial dimensions. The Alternating Direction method is an operator splitting method and is easier to work in higher dimensions than the Crank-Nicolson method.

2.1.6 Bursting in Discrete and Continuous Networks

Extended systems of coupled neurons, or neural networks, allow for a transmembrane potential difference to travel across multiple neurons by means of a propagating excitation wave. This process may result in syncronized electrical activity for groups of neighboring neurons. Such a synchronized excitation of neighboring cells, which is believed to play a central role in neural communication, is known as "bursting" [IBH05].

Bursting has previously been observed in discrete networks of mutually inhibitory oscillators [SKM94] and is responsible for pattern generation as seen within many different biological neural networks [MB01]. To investigate bursting, Skinner *et al.* used a Morris-Lecar-based network and explored inhibition through synaptic coupling by introducting Eq. 2.21 as a synaptic source

$$I_{\text{syn}} = m(\hat{V})(V - V_{\text{syn}}), \tag{2.21}$$

where I_{syn} is the synaptic current provided by the inhibitory neuron, $m(\hat{V})$ is a step-wise function which is zero below a particular voltage threshold and a positive constant above the threshold, and $\hat{V}$ is the voltage of the inhibitory neuron. It was demonstrated that such a coupling allows for frequency control analogous to

a neuromodulator where synaptic currents affect the intrinsic properties of single neurons as described in [HWM91].

Unlike the work of Skinner *et al.* we will investigate bursting regimes in a continuous reaction-diffusion system, where coupling between neuronal cells is introduced by a diffusion term in a nonlinear diffusion equation

$$\frac{\partial V(x,t)}{\partial t} = D\frac{\partial^2 V(x,t)}{\partial x^2} + f\left(V\right), \tag{2.22}$$

When a reaction-diffusion system is written in discrete form, suitable for numerical analysis, the effective coupling term (to second order) can be written in the form,

$$\begin{aligned} I_{\text{syn}} &= D\frac{\partial^2 V(x)}{\partial x^2}, & (2.23)\\ &\rightarrow \frac{D}{\Delta x^2}(V_{i+1} - 2V_i + V_{i-1}), & (2.24)\\ &= \frac{-2D}{\Delta x^2}(V_i - \left[V_{i+1} + V_{i-1}\right]/2), & (2.25)\\ &\equiv \Gamma(\hat{V})(V_i - V_{\text{avg}}), & (2.26) \end{aligned}$$

where $\Gamma(\hat{V})$ can be defined in terms of the diffusion constant D and spatial mesh size Δx in the way similar to the quantity $m(\hat{V})$ in Eq. 2.21. Previous work [AM97,AM99] has demonstrated the existence of soliton-like waves for specific voltage-dependent diffusion profiles. The link between these findings and neuronal bursting will be investigated in Section 2.3.

2.2 Morris-Lecar Model with Adaptive Nernst Equilibria

A variable Nernst potential across one or more ionic channels can be incorporated into Eq. 2.6 by introducting a shift, V_δ , as

$$C\dot{V} = -G_{\text{eff}}(V - [V_{\text{eq}} + V_\delta]). \tag{2.27}$$

The total trans-membrane potential difference from equilibrium, $(V - V_{\text{eq}})$, can be considered as the driving force of this nonlinear system. As the trans-membrane potential difference increases, the amount of charge stored on the cell surface also increases. This causes the concentration of intracellular ions to decrease, resuting in an elevated Nernst potential for positive ions. Using the Nernst equation [PB07] one finds the leading-order correction to the Nernst potential V_i of a single channel due to significant charge depletion $\delta = \Delta Q_i/Q_i$ to be,

$$\Delta V_i \approx -\frac{RT}{z_i F}\left(\frac{\Delta Q_i}{Q_i}\right), \tag{2.28}$$

where ΔV_i is the Nernst shift for the ith ionic channel, R is the ideal gas constant, z_i is the charge value for the ith ionic channel, T is temperature (assumed constant), and F is Faraday's constant. Any flux of charge leaving or entering through the cell membrane is a result of the total potential difference across the membrane surface,

$$\Delta Q_i \propto (V - V_{\text{eq}}). \tag{2.29}$$

Thus, for each ionic channel, the Nernst shift will be proportional to the total trans-membrane potential difference. Because this is true for any ionic channel with variable

Nernst potential, the average or effective Nernst shift, V_δ, will also depend on the total trans-membrane potential,

$$V_\delta = \alpha(V_0 - V), \tag{2.30}$$

where α and V_0 are constant parameters. Letting ζ represent the ratio of the average Nernst shift to the total trans-membrane potential,

$$\zeta = \frac{V_\delta}{(V - V_{\text{eq}})}. \tag{2.31}$$

Conservation of charge in a conductance-based model with variable Nernst potential in the form described by Eq. 2.27 and Eq.2.30 can thus be written as,

$$C\dot{V} = (1 - \zeta)[-G_{\text{eff}}(V - V_{\text{eq}})] + I_{\text{app}}. \tag{2.32}$$

A similar type of modification has been studied in the Fitzhugh-Nagumo model, where a "soliton-like regime" was discovered [AM99]. The connection of the present work to the soliton-like regime in the Fitzhugh-Nagumo model is explored in Sec. 2.4. To provide a context for single-cell and network simulations, Eq. 2.32 was applied to the two-variable version of the Morris-Lecar model [ML81]. When modified using Eq. 2.32, the Morris-Lecar system given by Eqs. 2.9-2.10 becomes,

$$\begin{aligned} C\dot{V} &= (1 - \zeta)[-G_{\text{eff}}(V - V_{\text{eq}})] + I_{\text{app}}, & (2.33) \\ \dot{W} &= (W_\infty - W)/\tau_W, & (2.34) \end{aligned}$$

with Eqs. 2.11-2.15 unchanged. Note that rather than being specific to the Morris-Lecar model, Eq. 2.32 represents a general method for incorporating a voltage-dependent Nernst equilibrium into any conductance-based, or Hodgkin-Huxley-like model. We have chosen to explore these effects using the Morris-Lecar model for its convenient balance between mathematical simplicity and biological relevance. While not as detailed as the Hodgkin-Huxley system, its parameters are based on biological quantities and not commonly viewed as arbitrarily tunable parameters. However, as a two-variable system the Morris-Lecar model shares a qualitative simplicity with other mathematically idealized models such as the Fitzhugh-Nagumo system.

2.3 Investigations into Single-Cell Dynamics and the One-Dimensional Excitable Cable

2.3.1 Single-Cell Dynamics

In this section, we wish to explore some basic properties of the Morris-Lecar system with the addition of an adaptive Nernst equilibrium by examining the equations governing a single excitable cell. While the context of the present work lies in studying behavior of neurons in the brain, we shall employ the standard Morris-Lecar parameters as a way to demonstrate the substantial effects caused by the introduction of a variable Nernst potential while minimizing the number of free parameters. The implications of our results outside of the usual domain of relevance for the Morris-Lecar model are discussed in detail in Sec. 2.5, but we note here that the present goal is a demonstration of the wide variety of interesting behaviors that can be captured with a continuous reaction-diffusion system which has been suitably modified to incorporate the dominant physical effects due to small cell size.

As a starting point, we refer the reader to Fig. 6, which shows the generic behavior observed in the conventional Morris Lecar system. Briefly, an external stimulation current can be applied to raise the membrane potential V above the model's threshold at which a rapid rise in potential (the "upstroke") occurs, causing an increase in the potassium current. This rising potassium current brings the membrane potential back down (the "downstroke"), overshooting equilibrium and resulting in a recovery time ("refractory period") during which no further stimulation generates an action potential. This basic picture of an action potential event is characteristic of virtually all common models used to study electrical activity in cardiac and muscular cells, and we now wish to explore how this picture changes when the Nernst potential is allowed to vary due to the charge depletion expected to occur within smaller neurons.

Our modified system contains two free parameters, namely α and V_0. Solving Eqs. 2.33-2.34 at different points in (V_0, α) space reveals two qualitatively different regimes of behavior. A region exists where most initial conditions fall into a stable limit cycle without any external stimulation current. In this regime, the system exhibits "autogeneration" of excitations. Outside of this region, the system behaves qualitatively similarly to the standard Morris-Lecar model given in Eqs. 2.9-2.10. An example of the time-series $V(t)$ and phase space (V, W) is shown for each of these regimes in Fig. 10.

While a complete characterization of this modified system is beyond the scope of the present work, we sketch a global aspect of the qualitative behavior in Fig. 11 where the natural resonant frequency is shown as a function of position in (V_0, α) space.

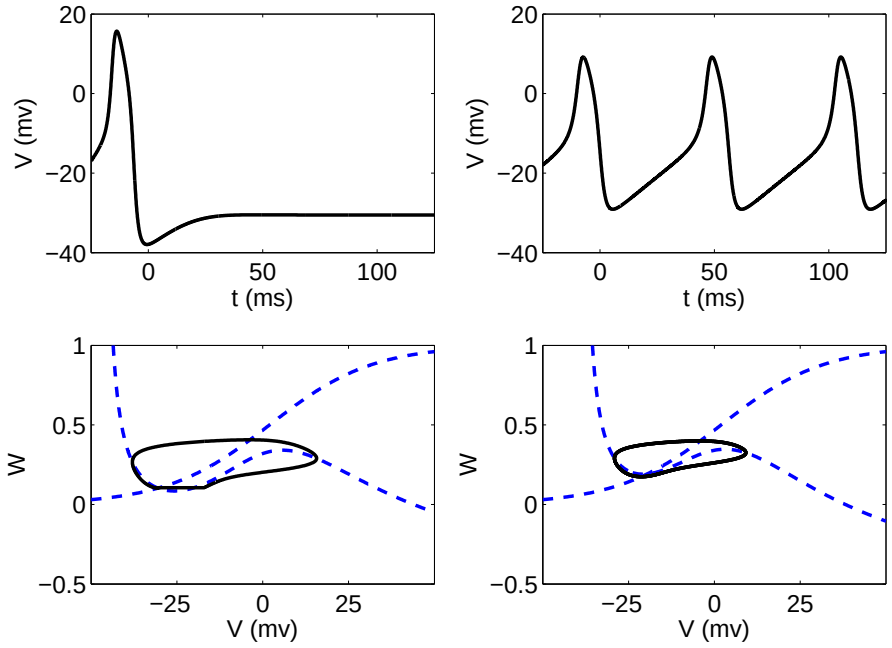

Figure 10. Morris-Lecar Phase-Space Dynamics. Upper left: Single neuron ($\alpha = 0.7$, $V_0 = 6.2$mV) firing once after stimulus is applied at $t = 0$ ms and approaching a stable equilibrium. Upper right: Single neuron ($\alpha = 1$ and $V_0 = 6.2$ mV) entering a stable limit cycle after initial stimulus. Phase space trajectories for each case are shown in the panel below the corresponding time-series plot.

The actual resonant frequencies depicted depend directly on the particular choices of parameters in Table. 3, but the for arbitrary choices of parameters, one may expect at least the order of magnitude in variation of resonant frequencies as both α and V_0 are varied over an order of magnitude in size over the resonant window.

The auto-generation of excitation pulses produced by Eqs. 2.33-2.34 is not entirely different from the behavior produced by the standard Morris Lecar model (c.f., Eqs. 2.9-2.10) in the presence of a constant stimulation current.

Indeed, a bifurcation diagram with respect to either α or V_0 demonstrates the emergence of a stable limit cycle within a range of values. Fig. 12 depicts these bifurcation diagrams which may be compared to the standard Andronov-Hopf bifur-

cation observed within the conventional Morris-Lecar model with respect to a varying stimulation current.

While mathematically similar, a distinguishing feature of the particular model presented here is that this regime of auto-generation emerges naturally within the extended parameter space of a model which includes the physical effects of small cell size. Specifically, these oscillations are driven by a Nernst potential which adapts to the instantaneous charge depletion experienced by the cell during an excitation pulse in lieu of an external current.

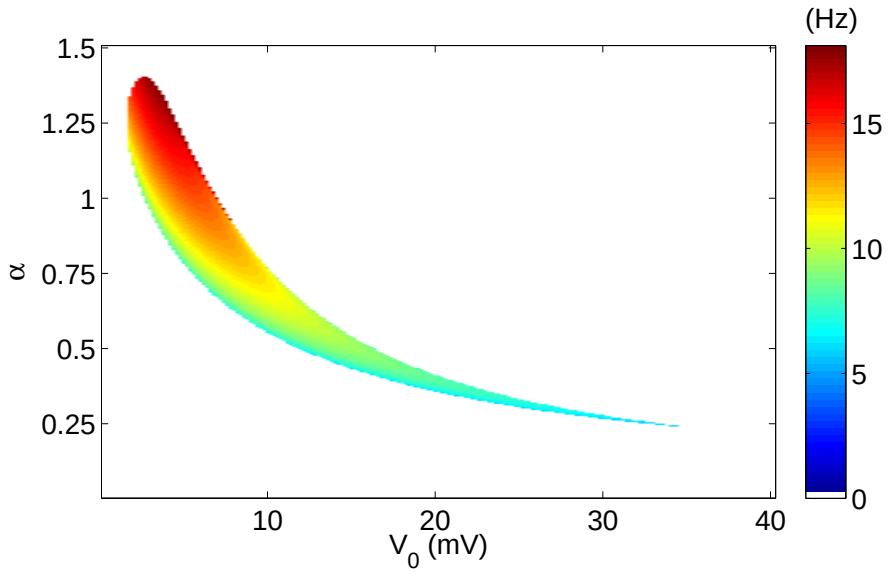

Figure 11. Resonant Frequencies for V_0 and Alpha. Map in (V_0, α) space of resonant frequencies using typical parameters for Morris Lecar model. Regions colored in white correspond to points where no stable limit cycles exist in the absence of a stimulation current.

As a last exploration of the single cell properties, we note that within the limit cycle, a range of stimulation currents may be applied within a particular phase window to send the system to a stable equilibrium point.

Fig. 13 depicts a stable limit cycle for a particular choice of (α, V_0) and how this dynamical behavior may be modified when a stimulation current is applied at a certain point in the cycle. Within this "vulnerable" phase window, a sufficient stimulation current can prevent further excitation pulses and cause the membrane potential to asymptotically approach a constant value, as shown in the right panel of Fig. 13.

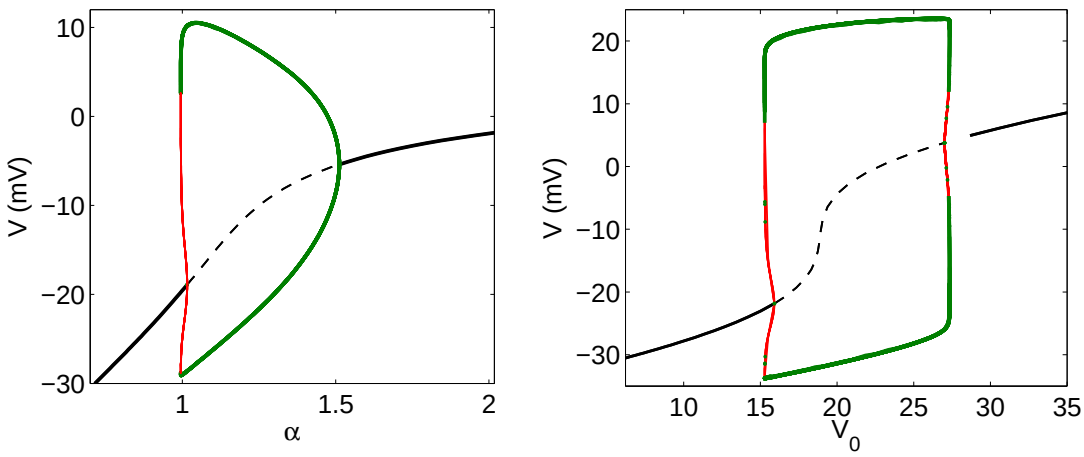

Figure 12. V_0 and Alpha as Bifurcation Parameters. Bifurcation diagrams created using XPPAUT showing occurrence of stable, equilibrium points (solid black line), unstable equilibrium points (dashed black line), stable limit cycle (thick green line) and unstable limit cycle (thin, red line) as α (left) and V_0 (right) are varied.

To fix this notion of a vunerable window, we may repeat the calculation leading to Fig. 13 for a fixed stimulation current protocol while varying the point in phase space at which the stimulation is applied. The range of phase space over which this particular stimulation protocol is effective in stabilizing the system is shown in Fig. 14. While we have chosen a particular stimulus protocol and varied phase, the general picture of a "vulnerability window" is quite robust and emerges within a measurable fraction of the phase space as a range of vulnerability with respect to variation in any particular parameter of interest.

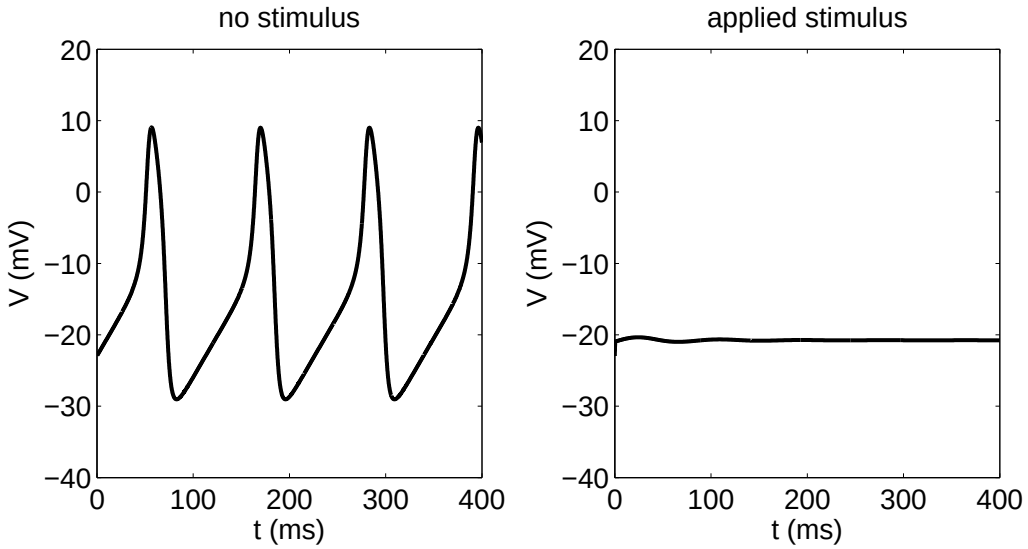

Figure 13. Single-Cell Dynamics. Left: Auto-generation of pulses in modified Morris-Lecar system with $\alpha = 1$, $V_0 = 6.2$mV. Right: An initial stimulus of 80 μA/cm^2 applied for 5ms is sufficient to pull the system off the limit cycle to a stable equilibrium.

In the next section, this notion of vulnerability is extended to the context of a one-dimensional cable of excitable tissue and explored as several size-related parameters are varied.

2.3.2 One-Dimensional Excitable Cable

In this section, we investigate the consequences of the window of vulnerability, depicted in Fig. 14, when the cell being stabilized is coupled to a chain of excitable cells by a diffusive term. As we shall demonstrate, this notion of "vulnerability" extends naturally to a one-dimensional cable through a range of parameter values which allows a localized stimulation to stabilize an entire, synchronized cable.

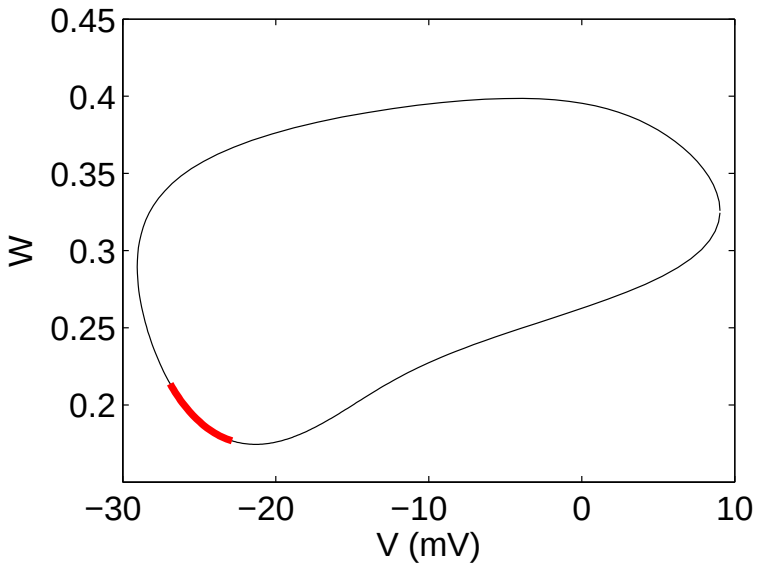

Figure 14. Vulnerable Window in the Modified Morris-Lecar Model. The system's limit-cycle trajectory for $\alpha = 1$, $V_0 = 6.4$mV is shown (thin black line) with the vulnerable region indicated by a thick red line. Within the vulnerable window, a short stimulation takes the system from its stable limit cycle to a stable equilibrium point in phase space.

Regarding the experimental relevance of such a vulnerability window in extended systems, previous research has demonstrated the existence of a soliton-like regime close to a subcritical Hopf bifurcation point. Analysis using the Hodgkin-Huxley model predicts this regime to exist within a 0.1 mM concentration window of extracellular potassium. Below this concentration one generically observes standard action potential propagation. Above this region one observes pulse trains of propagating action potentials, which are likely contributors to seizure-like activity. A shift from the single-fire regime to the soliton-like regime, with pulse trains of action potentials, is typically pathophysiological.

Given the clear role action potentials play in formation of memory [AMF+06a], we are also interested in the possible patterns one could find within this soliton-like

regime, for which small diameter axon activity would likely reside. Using the modified Morris Lecar model, we present a fundamental, biologically-based, mechansim for spatiotemporal pattern generation.

For our investigation of extended excitable media, we will consider a continuous cable of excitable tissue governed by,

$$C\dot{V} = D\frac{\partial^2 V}{\partial x^2} + (1-\zeta)[-G_{\text{eff}}(V - V_{\text{eq}})] + I_{\text{app}}(x,t), \tag{2.35}$$

$$\dot{W} = (W_\infty - W)/\tau_W. \tag{2.36}$$

Normally, the system of Eqs. 2.35, 2.36 has a simple excitation pulse solution in response to an external stimulus. If α and V_0 are selected close to an Andronov-Hopf bifurcation point we obtain one stable equilibrium and two limit-cycles (one stable, one unstable) simultaneously [Izh10] for each cell in the cable, as shown in Fig. 12. A particular consequence of each cell lying close to this bifurcation point is a global vulnerability of the entire cable with respect to localized stimulations. To demonstrate this global vulnerability, we consider a cable of length L undergoing synchronized oscillations (i.e., each cell in the cable is oscillating in phase with frequency given by Fig. 11) and apply a short stimulation current near the center of the cable at a particular phase of the oscillation. Henceforth, we fix our initial conditions to be $V(t=0,x) = V_0$, $W(t=0,x) = W_0$, with

$$V_0 = -22.9764\text{mV}, \tag{2.37}$$

$$W_0 = 0.1770. \tag{2.38}$$

The diffusion constant is fixed to $D = 0.01\text{cm}^2/\text{s}$ unless otherwise noted, and we take $L = N_x \Delta x$ to be the length of the cable, where N_x is the number of spatial points considered.

Fixing $\alpha = 0.6$ and $V_0 = 1\text{mV}$ as a representative point in (α, V_0) close to the system's Andronov-Hopf bifurcation point, we proceed to first demonstrate that a fixed stimulation current is able to de-synchronize an entire, extended cable for a fixed range of cable lengths. Fig. 15 schematically depicts this window of vulnerablity by applying a stimulation current of amplitude $i_0 = 100\mu\text{A}/\text{cm}^2$ for a duration $T_0 = 1000\Delta t$ to the center cell and its three nearest neighbors to the right and left for a total of seven cells. For both sufficiently large and sufficiently small cables, a stimulus sufficient to stabilize a single cell is unable to counteract the cell's coupling to its oscillating, neighboring tissue (left and right panels of Fig. 15), and the system returns to a synchronized limit cycle. However, for a range of cable lengths, the initial stimulus results in a fully quiescent region which eventually spreads throughout the entire length of the cable (center panel). This resonant effect occurs for a small range in values of L given all other parameters fixed.

In the continuum limit, with which we are interested, the diffusion constant we have introduced is scalable in the sense that a change in D for a system of length $L = N_x \Delta x$,

$$D \to D', \tag{2.39}$$

should result in spatiotemporal dynamics equivalent to those in a system of size

$$L' = L \left(\frac{D}{D'} \right)^{1/2}. \tag{2.40}$$

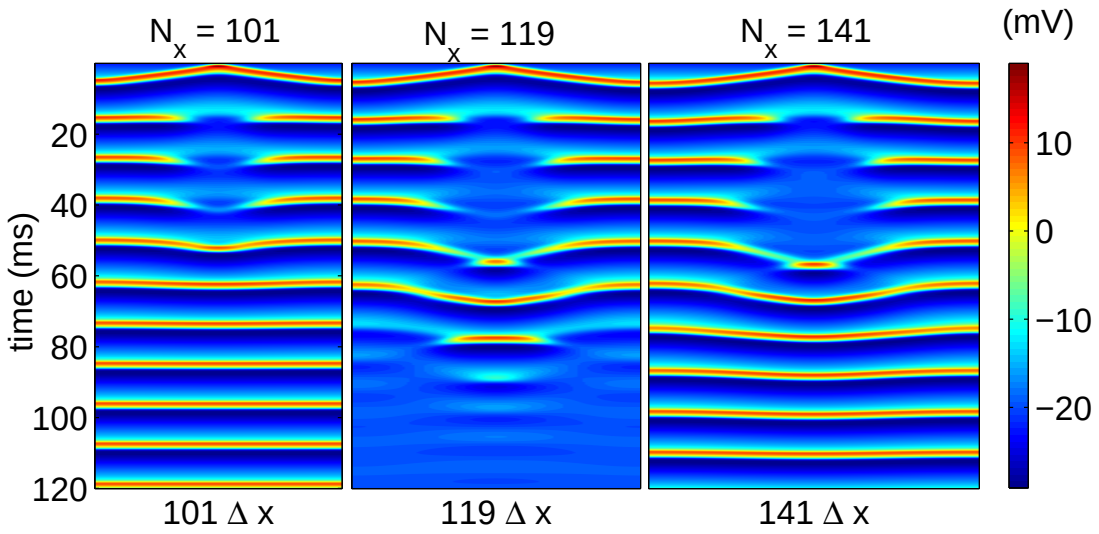

Figure 15. One-Dimensional Cable Dynamics. Fixing all parameters except cable length generically yields a region of vulnerability in extended cables. For small (left) and large (right) cables, an initial stimulation sufficient to quiesce a single cell causes a transient quiescent region which results in full synchronization. For a range of cable lengths (center) the stimulation results in the entire cable approaching an equilibrium state.

To demonstrate that we are considering discretized systems that effectively represent the continuum limit, we may test this scaling by holding $L = N_x \Delta x$ fixed and varying D in a manner that should reproduce results equivalent to those depicted in Fig. 15. The results of this variation in diffusion constant are shown in Fig. 16 and support the claim that, by comparison to Fig. 15, these results genuinely represent an accurate description of the continuum limit.

While adjusting the diffusion constant does not itself represent a truly independent variation of system properties, we can demonstrate the robustness of our results by modifying the stimulation protocol. The nature of the window of vulnerability is fairly insensitive to changes in the nature of the stimulation, provided the overall charge $Q = i_0 \Delta t$ is sufficiently large.

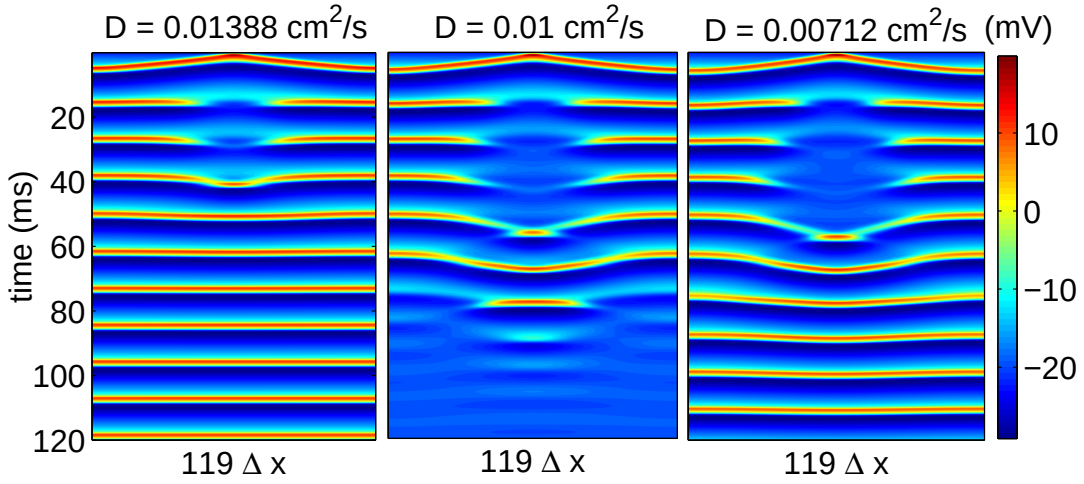

Figure 16. One-Dimensional Cable Dynamics. Variation of diffusion constant shows results consistent with the continuum predictions. Compare to Figure 15.

Fig. 17 shows a picture qualitatively similar to that in Fig. 15, produced with a larger stimulation current, $i_0 = 800\mu\text{A/cm}^2$, applied for a shorter time $T_0 = 50\Delta t$.

The general behavior of the model within the regime we have focused is fairly straightforward. As with the single cell, when α and V_0 are chosen close to the Hopf bifurcation point (close to the edge of the cloud showing nonzero resonant frequencies in Fig. 11) and a stimulation is applied within the vulnerable phase region (see Fig. 14) in a localized region at the center of an extended, one-dimensional cable, there exists a range of lengths for which the entire cable becomes quiescent due to the stimulation. Outside of this range, for both smaller and larger cable lengths, the synchronized oscillations overtake any transient, quiescent behavior. By varying the oscillation phase at which the stimulation is applied and holding all other parameters (cable length, stimulation strength, etc.) fixed, one may construct a global vulnerability picture for the entire cable as was done for the single cell in Fig. 14.

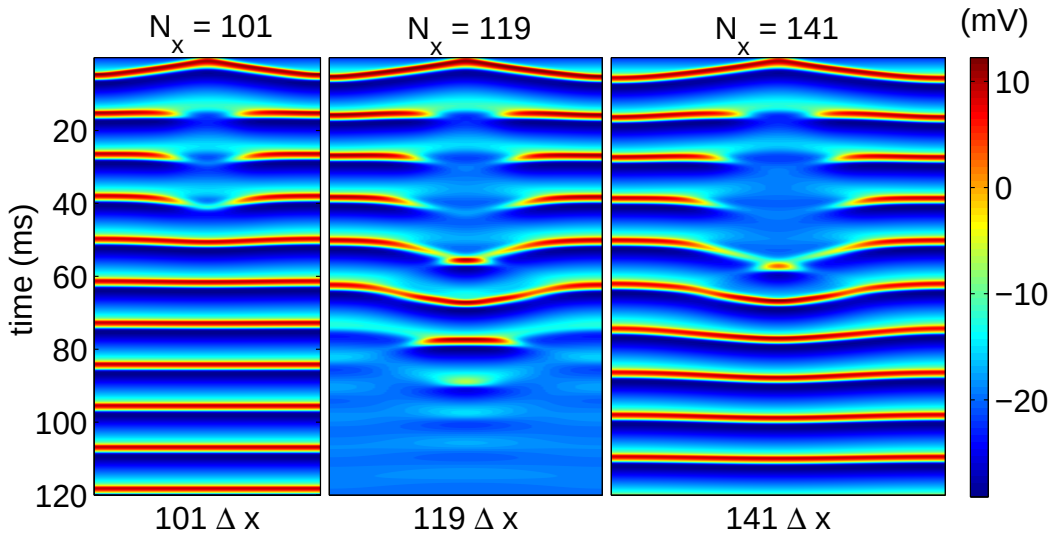

Figure 17. One-Dimensional Cable Dynamics. Larger stimulation current ($i_0 = 800\mu\text{A/cm}^2$) is used for a shorter time ($T_0 = 50\Delta t$) in the middle of the cable, producing qualitatively similar results to those shown in Figure 15.

The global vulnerability picture for $N_x = 119$, $i_0 = 100\mu\text{A/cm}^2$, $T_0 = 1000\Delta t$ is shown in Fig. 18, and the basic picture is quite similar to that for a single cell. Specifically, a small window of phases exists at which a stimulation may be applied resulting in the entire cable transitioning from synchronized oscillations to a homogeneous, quiescent state. Far away from this window, the effects due to the localized stimulation are transient, and the cable returns to synchronized oscillations at long times. However, a new layer of complication is introduced by the spatial extension of the one-dimensional system. In the region of the transition between these two types of long-time steady states, the system shows extreme sensitivity to the particular details of stimulation. Moreover, numerical instabilities arise that make an accurate description of the system at long times practically impossible. The region of phase at which a stimulation gives rise to complex instabilities is shown by the dashed blue line in Fig. 18.

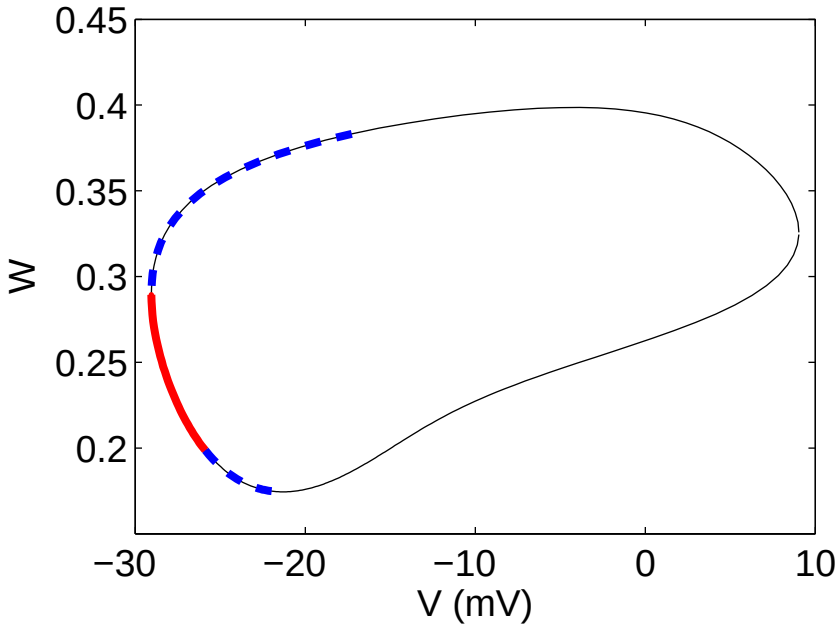

Figure 18. Vulnerable Window of the Modified Morris-Lecar Model. The system's limit-cycle trajectory for $\alpha = 1$, $V_0 = 6.4$mV is shown (thin black line) with the vulnerable region indicated by a thick red line. Regions of instability are shown in dashed blue line.

As an example of the interesting types of behavior lurking within this unstable regime, Fig. 19 depicts some extremely long-lived transient behavior. In this case, the cable is extremely sensitive to the time T_0 during which the stimulation is applied with small changes in T_0 corresponding to dramatic changes in the long-time steady state. The persistence of this transient spatiotemporal complexity for long times (tens of oscillations, as shown in Fig. 19) makes an accurate investigation of the dynamics governed by the highly nonlinear partial differential equations, Eqs. (2.35)-(2.36) practically quite difficult.

The possibility of generating such complex spatiotemporal patterns as those shown in Fig. 19 is intruiging in its own right.

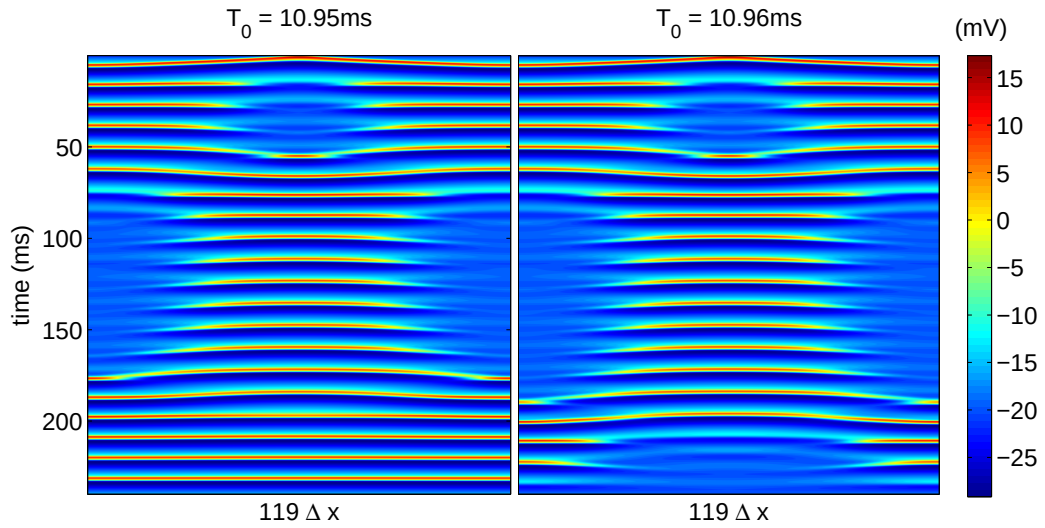

Figure 19. One-Dimensional Cable Dynamics. Complex spatiotemporal pattern generated with increased stimulation time near the crossover between quiescent and synchronized steady-states A standard, second-order stencil was used for evaluation of the spatial derivative.

However, another interesting aspect of this complexity may be seen by considering the time-series for the membrane potential of a single cell. Fig 20 depicts the membrane potential as a function of time for the center cell in the right-hand panel of Fig. 19.

The shape of $V(t)$ in Fig. 20 is remarkably similar to bursting behavior, which is typically by introducing a third dynamical variable to a two-variable system such as the Morris-Lecar model. Through the propagation of voltage through the extended medium and the complex dynamics generated with the adaptive Nersnt-potential, our model shows the potential to capture bursting. Abstractly, one may think of our (effective) "third equation" as the integrated effects of coupling the center cell to the rest of the cable.

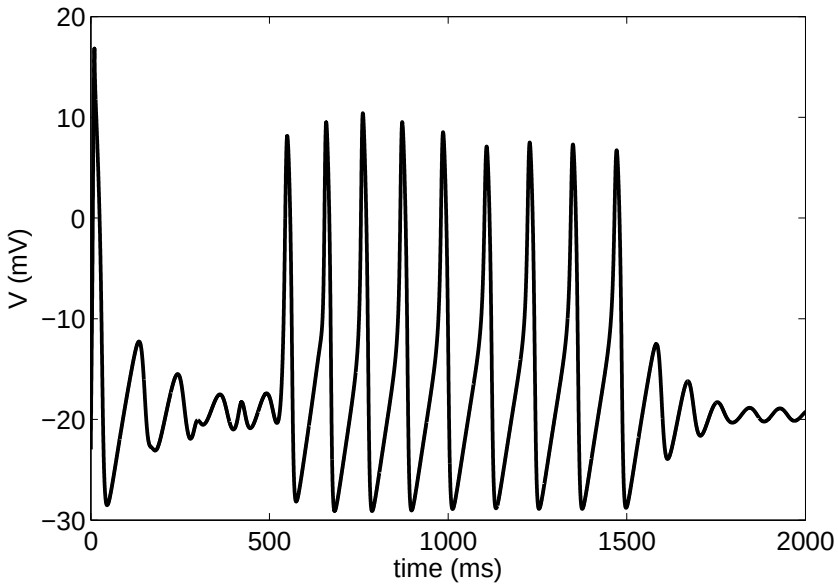

Figure 20. Single-Cell Bursting. Time series for the membrane potential V at the center cell in the one-dimensional cable shown in Figure 19.

Unlike other conventional models for bursting [DZ11, AFR13], we find bursting to arise in this intrinsically two-variable system through coupling of the cell to an extended system.

2.3.3 Numerical Details

For numerical solutions of Eqs. (2.35)-(2.36), we discretize space and time by taking mesh sizes of $\Delta x = 0.1$cm and $\Delta t = 0.01$ms for spatial mesh and time-integration step size, respectively. Time integration is performed using an explicit, fixed step-size, fourth-order Runge Kutta method. The spatial derivative is approximated by the standard second-order stencil,

$$\frac{\partial^2 V}{\partial x^2} \to \frac{1}{\Delta x^2}\left(u_{j+1} + u_{j-1} - 2u_j\right), \tag{2.41}$$

with a fourth-order, five-point stencil [oS64] used to confirm all results displayed in this section. When using explicit integration schemes, the numerical stability of a linear diffusive system is governed by the Courant-Friedrichs-Levy (CFL) number, which should satisfy $\mu \ll 1$ to ensure a numerically stable solution.

$$\mu = \frac{D\Delta t}{\Delta x^2}, \tag{2.42}$$

We find experimentally that even for $\mu \ll 1$, the solution is extremely sensitive to changes in step sizes due to the nonlinear nature of the system which precludes a strict application of linear stability analysis. To check the accuracy of solutions presented in this paper, all solutions were computed with a variety of spatial and temporal step sizes, Δt and Δx, respectively, while holding cable length L and overal integration time T fixed. Additionally, a fourth-order, five-point stencil was employed for the diffusive term in Eq. (2.35) and compared to results obtained from a standard second-order, three-point stencil. Aside from Figs. 19-21, no difference was observed when varying step sizes or spatial stencil. In the transitional regime, however, simply changing the spatial stencil resulted in significantly different behavior. Qualitatively similar behavior to that shown in Fig. 19 exists when the modified stencil is employed, but the particular value of T_0 at which it occurs is slightly different when the higher-order stencil is used, as shown in Fig. 21.

Regardless of the particulars of the numerical parameters used to obtain approximate solutions, the behavior depicted in Fig. 19 is robust in the sense that it can generated for some particular form of the stimulation protocol. While such delicate behavior is extremely difficult to investigate rigorously within the context of a

highly nonlinear, continuous reaction-diffusion system, these results have immediate relevance to inherently discrete systems where the diffusive coupling

$$\Delta t D \frac{\partial^2 u}{\partial x^2} \rightarrow \frac{\Delta t D}{\Delta x^2} \left[u_{j+1} + u_{j-1} - 2u_j \right], \tag{2.43}$$

$$\equiv \Gamma \left(u_{j+1} + u_{j-1} - 2u_j \right), \tag{2.44}$$

becomes a synaptic coupling between discrete neurons with a well-defined value. In this context, the numerical instability we see corresponds to a dramatic sensitivity of system behavior on the particular coupling between neighboring cells.

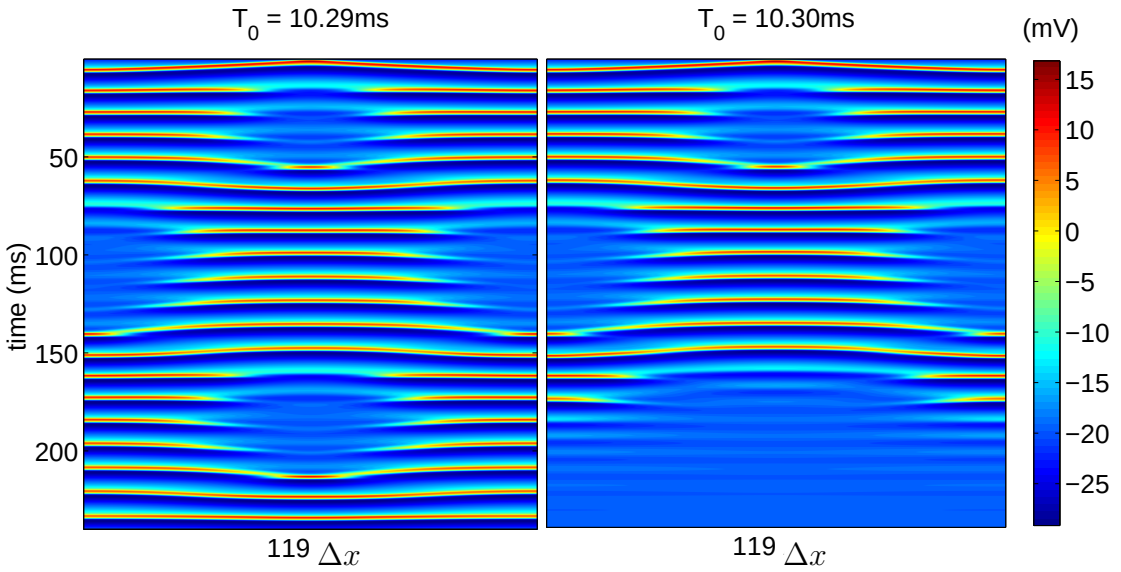

Figure 21. One-Dimensional Cable Dynamics. Complex spatio-temporal pattern generated with increased stimulation time near the crossover between quiescent and synchronized steady-states A fourth-order, five-point stencil was used for evaluation of the spatial derivative. Compare to Figure 19.

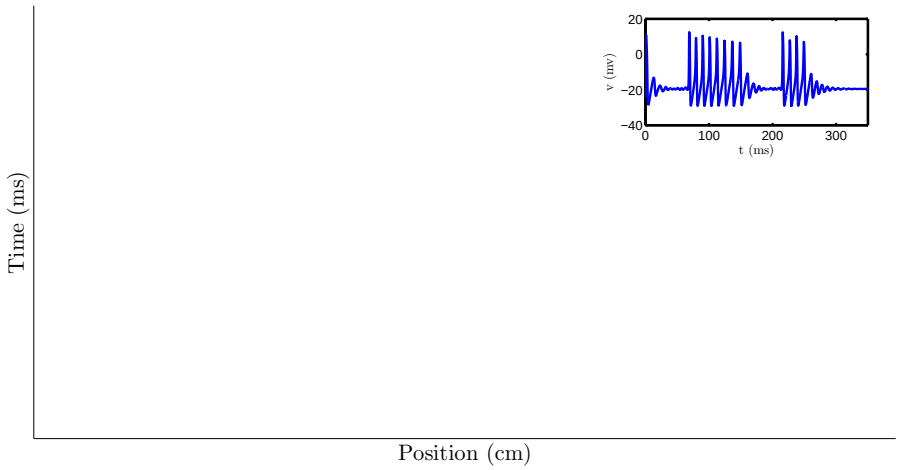

Figure 22. Bursting in a One-Dimensional Cable. This plot shows single-cell bursting (inlay), at the cable's center point, as a result of communication between spatially separated neurons in a one-dimensional cable.

2.3.4 Network Bifurcations and the Soliton-Like Regime

One excellent example of bursting within a network of neurons is the release of oxytocin during lactation [WLL+12].

Neuroendocrine cells receive a neuronal input (via suckling) and release the oxytocin hormone into the blood causing milk let-down in lactation. Action potentials are responsible for the secretion of oxytocin and during suckling intense bursts of action potential followed by periods of quiescence release pulses of oxytocin into circulation [RFT+08].

Bursting has also been observed in rodent trigeminal neurons [NHCG98] and dorsal root ganglion [LYL+12] as well as many other neural networks. A review is provided by Izhikevich [Izh10]. To see the similarities between bursting in a simulated continuous network and a measured experimental result compare Fig. 7 with the inlay in Fig. 22.

At the left and right ends of the fiber in Fig. 9 we see heightened potential values which are indicated by the dark red regions in the color contrast. These regions of heightened potential are due to our imposed ion impermeable boundries (no-flux boundries). Since ions are unable to escape, they collect by the boundry causing an increase in ion density.

These regions of high ion density are no different than regions where an external current is being applied, except that the current amplitude is dependent on the incoming action potential. In 1999 Aslanidi and Mornev noticed that propagating action potentials could be made to reflect off no-flux boundries if the local intrinsic dynamics of cells at the boundry occurred in the vicinity of a Hopf bifurcation [AM99].

The result obtained by Aslanidi and Mornev is a natural extension of this idea when we consider the no-flux boundry to act as an applied current. Meaning that if the cells located by the no-flux boundry are close to producing a Hopf bifurcation (i.e. producing a stable limit-cycle) then the current provided by the no-flux boundry is enough to produce a stable limit-cycle at the boundry. This effective current only exists while the density of ions is high, which is often long enough for a single backwards propagating action potential for form. The same behavior exists when two propagating action potentials with similar voltage profiles collide (i.e. due to symmetry and the natural no-flux boundry at the collision point). In the literature this behavior is often termed as being soliton-like and is the term used by Aslanidi and Mornev in describing this phenomena.

Here we see local bifurcation events having a huge impact on global network dynamics. The intrinsic properties of the cells within the network and their positions

determine what we see on a larger scale. In Chp. III we look at multifractal analysis as a metric for information encoding and how it could provide a means for measuring a neuron's functional utility.

2.4 Derivation of the Soliton-Like Regime in the Fitzhugh-Nagumo Model

Mornev and collaborators [AM99] considered a modified form of the Fitzhugh-Nagumo equations,

$$\frac{du}{dt} = f(u) - v, \tag{2.45}$$

$$\frac{dv}{dt} = \epsilon_0 g(u)\left[\zeta u - v\right], \tag{2.46}$$

where $f(u) = (u - m_0)(u - m_1)(u - m_2)$, and $\epsilon(u)$ was chosen to be

$$g(u) = \left(1 + \lambda\left[2 - \tanh\left[(u + 0.04)/0.01\right] + \tanh\left[(u - 0.75)/0.1\right]\right]\right), \tag{2.47}$$

for some constants ϵ_0 and λ. Rescaling the time variable according to

$$d\tau = g(u(t))\, dt, \tag{2.48}$$

Eqs. (2.45)-(2.46) become

$$\frac{du}{d\tau} = \frac{1}{g(u)}\left[f(u) - v\right], \tag{2.49}$$

$$\frac{dv}{d\tau} = \epsilon_0\left[\zeta u - v\right], \tag{2.50}$$

so that with rescaled time, the u-dependence introduced to ϵ, responsible for the behavior characterstic of the "soliton regime" examined by Mornev and collaborators, can be recast in the form of an effective shift in Nernst potential by the identification

$$\frac{1}{g(u)} \to 1 - \zeta, \tag{2.51}$$

where in the ζ is a ratio of two linear functions of u, according to Eqs. (2.30)-(2.31), and u plays the role of V in the Fitzhugh-Nagumo system. Performing a Taylor expansion of the hyperbolic functions around $u \approx -0.04$ or $u \approx 0.75$ reduces $g^{-1}(u)$ to the same functional form as $1-\zeta$, indicating that the "soliton-like" effects observed by Mornev and collaborators [AM99] can be understood from a physiological perspective as a result of an adaptive Nernst potential which becomes more pronounced in its effects for smaller excitable cells. It should be noted that Mornev [AM99] also introduced nonlinear diffusion to the Fitzhugh-Nagumo model which is not described within the framework we have presented. Preliminary computations indicate that the nonlinear diffusion considered in Ref. [AM99] is not essential to capturing many aspects of the soliton-like regime including reflection from open boundaries. Systematically incorporating further complications to our model is a direction for future research.

2.5 Summary and Conclusion

In this chapter we have presented a physically motived modification to excitable models based on the charge depletion which occurs in small excitable cells, such as neurons. By incorporating this modification into the conventional Morris-Lecar model, we have explored several examples of the emergent complex behavior which

have particular relevance to synchronization of neurons in the brain and the relevance of synchronization to diseases such as epilepsy. The Hodgkin-Huxley system and related models are currently the closest representation we have to the actual biological processes taking place within the membrane of an excitable cell.

Generalizing these reaction-diffusion models to include dynamical Nernst potentials provides a platform for future investigation into what diffusive chemical influences may have on neural network dynamics. Seizure activity and various bursting events are heavily influenced by external factors. If preliminary information regarding medicinal reactions are known, these effects could possibly be incorporated within a reaction-diffusion system by means of profiled diffusion. Recent research into Belousov-Zhabotinsky reactions and chemical computing [RKM98] show a promising future for understanding how information is retrieved and written within networks such as these. Being able to better understand how these networks are maintained could one day allow us to store and transfer data to an extent never before realized. In addition to providing benefits to those suffering from mental illness, understanding neural network stability could also provide new ways of encrypting sensitive network information.

Research on epilepsy and seizures has shown that a neuron will swell as a result of electrical activity and when modeling such activity one must account for variations in ion concentration [CUZ+09]. By incorporating this dynamic size variation into network simulations it was shown that if glial cells fail to maintain the proper micro-environmental conditions neurons will produce seizure-like activity. It was also suggested that how persistent states respond to perturbations may be critical to transient behavior such as working memory [UJBS09]. One could hope that in the

near future our understanding of neural networks will allow for a more quantitative understanding of complex brain activity such as working memory.

In the work of Mornev and Aslanidi [AM99, AM97], soliton-like behavior, with reflection from zero-flux boundaries, was observed in addition to complete synchronization of the cable. The ratio of time constants for membrane potential and recovery was shifted by a function of trans-membrane potential but without any obvious physiological reason. The present work is an extension of this type of investigation with the aim of better understanding the particular nonlinearities responsible for observable phenomena and strengthening the link between mathematics and physiology. In agreement with Aslanidi and Mornev we observed elevated ion fluxes in proximity to the ion impermeable, no-flux, boundaries. Therefore, one would expect, for fibers where the size of the stimulation site is comparable to length of the fiber, these no-flux boundaries would reinforce the current applied at the site of stimulation. This is in agreement with what we observed for smaller cables where the entire fiber remains synchronized with a simple phase-shift in accordance with the stimulus applied. That is, if the size of the stimulation site is relatively large in comparison to the fiber length, the no-flux boundaries will work to amplify the applied stimulus so that the fiber becomes indistinguishable from the situation where one would apply a stimulus to the entire fiber itself.

However, when the fiber is long to produce effective causual separation between the center and edges, yet short enough so that the interplay between the center stimulus and elevated ion-fluxes at both ends of the fiber may produce long-lived, transient behavior, we find an alternation between establishing a phase difference and complete quiescence. Interestingly, this is also the regime where pattern formation

was observed. The open boundaries act as impermeable membranes so that the fiber becomes isolated, and acts as a one-dimensional pathway for voltage disturbances. As demonstrated by Aslanidi and Mornev, if a cable is composed of cells tuned to be near a Hopf Bifurcation point, it is possible for the elevated ion-concentrations located at the fiber's edge to cause reflections at the open boundaries. Therefore, these isolated regions may sustain activity without external influence. When a stimulus is applied to these isolated regions, as would be the case for sensory information being delivered to information processing units within the brain, the transients may form complicated patterns. Most interestingly, when a single cell of the fiber is monitored we observe potential curves (c.f., Fig. 20) qualitatively identical to bursting measurements made in rat brains [NHCG98].

The results in this chapter suggest soliton-like regimes are likely common in biological, excitable media. Additionally, we find that one need not abandon the Hodkin-Huxley-like, parallel channel framework to observe such regimes. An interesting open question concerns the role played by the phase of stimulation plays in pattern formation. Examining the phase-response for single cells close to a Hopf bifurcation point, one finds the existence of a stable limit-cycle, unstable limit-cycle, and a stable equilibrium point. If the initial conditions are such that the cell is undergoing stable limit-cycle oscillations and a stimulus is applied within the hyperpolarization stage of cell recovery so that the trajectory moves across the unstable limit-cycle, then the stimulation will result is a quiescent cell. Based on these observations the notion of a "vulnerable window" was established. This compact picture of a vulnerability window represents a sort of building block to which further research may add in the

construction of systems used to describe memory formation and both physiological and pathophysiological behavior within such systems.

CHAPTER III

THE RELATIONSHIP BETWEEN NERNST EQUILIBRIUM VARIABILITY AND THE MULTIFRACTALITY OF INTERSPIKE INTERVALS IN THE HIPPOCAMPUS

3.1 Background

The brain is estimated to contain 100 billion neurons and 100 trillion synapses [WH88]. The brain is subdivided into many different regions, with the hippocampus region primarily recognized for memory processing [SM57]. The hippocampus itself is further divided into smaller regions, with the most experimentally explored regions being the CA1 and CA3 regions. Action potentials (spikes) travel from the CA3 region of the hippocampus along Schaffer collaterals toward the CA1 region [CGAO98]. Pyramidal neurons provide the infrastructure for signal propagation within these regions of the hippocampus. The time interval between successive spikes for a single neuron is referred to as the interspike interval (ISI). Consecutive ISIs are only correlated when biological information persists from one spiking event to the next. Quantifying these correlations gives some indication for the memory capacity of the neuron. The Hurst exponent is a quantitative measure for signal correlation and is commonly used to assess how statistical properties scale in time series data [Ihl12]. Eq. 3.1 shows the relationship between the correlation function, $c_q(x)$, for the q^{th}-order statistical moment and the generalized q^{th}-order generalized Hurst exponent (the Hölder exponent), H_q. The generalized Hurst exponent is preferable when working with non-stationary data sets such as experimentally recorded ISIs [BV91]. For

the 2^{nd}-order statistical moment (i.e. the variance) low exponential values correspond to mean-enforcing data, while high exponential values correspond to trend-enforcing data [QR04].

$$c_q(x) \sim x^{qH_q} \tag{3.1}$$

Several mechanisms are responsible for correlating ISIs in cortical neurons, most of which take place through a process known as spike-frequency adaptation. These mechanisms are categorized into two distinctive groups: low-threshold broad adaptation and high-threshold sharp adaptation. A good example of low-threshold broad adaptation is the slow voltage-dependent potassium current, whereas the calcium-dependent potassium current is often associated with high-threshold sharp adaptation [EPG01]. In addition, excitatory-inhibitory pairs in neuronal networks produce similar phase response curves (PRCs) as high-threshold adaptation in the excitatory neuron. Therefore spike-frequency adaptation is not relegated to only single-cell mechanisms but may also occur at the network level. In addition, whether the neuron is a resonator (Andronov-Hopf) or integrator (Saddle-Node) dramatically affects the correlation patterns of ISIs. Resonators possess a richer variety of ISI patterns than integrators [SL13]; although integrators, typically associated with Class I excitability (i.e. Saddle-node on invariant circle), possess a richer frequency band [Izh10].

The multifractality of ISIs has been linked to memory performance in rodents. Neurons with wide singularity spectra play a greater role in memory processing than neurons with narrow singularity spectra [FOS+14]. Pyramidal neurons in the CA1-CA3 regions of the hippocampus communicate with many other cells. However, the majority of these postsynaptic potentials (PSPs) have very low amplitudes. As a

result, these low amplitude PSPs work to keep the hippocampus pyramidal neurons in the vicinity of a bifurcation point [HI97]. Many interesting dynamics, including the soliton-like regime [AM99, MLS15], occur in the vicinity of bifurcation points.

In this chapter we investigate Nernst variability and its possible relationship with the multifractality of interspike intervals from neurons within the hippocampus. In Sec. 3.2 we discuss the various defining features of well-known models of neural activity. This discussion explains why it is particularly important to retain the some features of hippocampal neurons which impact correlations in ISIs. In Sec. 3.3 we discuss our computational methods for singling out the transient effects of charge depletion. Our technique ensures that differences in multifractality result from only the biological parameters which we are interested in addressing. In Sec. 3.4 we apply our model to experimental ISI data to investigate how the administration of various drugs can impact the ability for hippocampal neurons to process information. Our results show a clear distinction between various levels of Tetrahydrocannabinol (THC) and Cannabidiol (CBD) drug administration. These results suggest CBD may help prevent the short-term memory impairment effects of THC. In Sec. 3.6 we discuss various biological mechanisms that may impact the variability in the Nernst potential and how these mechanisms might contribute to memory processing.

3.1.1 Anatomy of the Hippocampus

The human brain has a left and right hippocampus, each located at the left and right ends of the fornix that runs along the middle region of the brain and branches downward. The hippocampus formation contains the entorhinal cortex, dentate gyrus, CA1 and CA3 areas, and the subiculum [EC04]. The subiculum is the main output component for the hippocampus and communicates with many other re-

gions of the brain [WG90]. Signal input for the subiculum comes from the CA1 region of the hippocampus where all portions of the CA1 region project to the subiculum [ADAR91]. Long-term potentiation (LTP), as a model of synaptic plasticity, was observed in the CA1-subiculum projection [CGAO98].

The hippocampus as a whole is important to spatial memory and reasoning. This is due to the signal interaction between CA3 and CA1 neurons. Within CA1 region of the hippocampus, certain neurons are labeled as 'place-related' depending on their electrically activity when rats are placed within regions which they know well. The subiculum does not contain these place-related cells and recent biological models predict this is because CA1 place-related cells converge to a substantial smaller number of cells during the project into the subiculum [O'M05].

It is of great theoretical interest to derive a set of applied currents which produce ISIs that mimic those found experimentally. Initial steps toward such a procedure are discussed in Sec. 3.3. Once the CA1 place-related cells have theoretical projections which adequately mimic the experimental ISIs, a study could be conducted which models the subiculum as a continuous network of neurons; similar to the reaction-diffusion system discussed in Sec. 2.3.2. Current biological literature suggests that place-related cells in the CA1 region of the hippocampus converge to a near single point on the subiculum [O'M05]. These projections could be used as inputs to the theoretical model of the subiculum in hopes to generate network transitions from single firing action potentials to synchronized bursting events. Such a result would provide a fundamental insight for which CA1 projections are required to turn on cortical circuit located elsewhere in the neocortex [SJT$^+$00].

3.2 A Physiologically Detailed Single-Compartment Model for CA1 and CA3 Principle Neurons

There are a few defining features of the CA1-CA3 neurons which we considered before designing our theoretical procedure. As previously mentioned, the patterns in ISIs depend on whether incoming pluses are capable of delaying the onset of future spikes. This corresponds to whether the phase response curve (PRC) of the model neuron has negative portions (Type II) or is strictly positive (Type I) [Erm96]. Neurons commonly referred to as *resonators* possess a Type II PRC, whereas neurons commonly referred to as *integrators* possess a Type I PRC. The PRC is strictly positive for integrators meaning incoming pulses may only advance the onset of future spikes, never delay them. Resonators are known to produce a wider variety of ISI patterns due to their subthreshold oscillations and ability to produced spikes from pulses of hyperpolarizing current [SL13].

Another distinctive characteristic to consider is the class of excitability [Hod48, RE89]. Class I excitability is characterized by arbitrarily low firing frequency when an injected current is applied. Class II excitability jumps in frequency and has a relatively narrow frequency band. Excitatory pyramidal neurons in the CA1-CA3 regions are generally Class I excitable whereas inhibitory interneurons within these regions are Class II excitable [Izh10]. Inhibitory interneurons make up about 10-20% of the neurons within the hippocampus and generally work to control information flow within cortical circuits [CT12]. Because of the wider frequency band, excitatory pyramidal neurons are able to encode input signal strength to output frequency and often have non-local projections whereas inhibitory interneurons work to control these signals and are more locally projected.

The crux to all these characteristic features described above is the phase plane dynamics; specifically, the type of bifurcations which are possible in phase space. Class I excitability is most amply associated with the Saddle-Node on an invariant circle bifurcation and Class II excitability is associated with the Saddle-Node (off-limit cycle) bifurcation as well as the subcritical and supercritical Andronov-Hopf bifurcations. Integrators (Type I PRC) are neurons with Saddle-Node bifurcations while resonators (Type II PRC) are neurons with Andronov-Hopf bifurcations.

After considering these various characteristics and the degree to which each influences the output ISIs, the soma compartment for the reduced Traub model of CA1-CA3 hippocampal neurons was used to model principal excitatory neurons in the hippocampal region [TWMM91,PR94]. This model follows directly from the well-known Hodgkin-Huxley formalism [HH52,KK73,TWMM91] for neuronal excitability and is well fitted to physiological data from hippocampal neurons; thus making it an excellent model for analyzing the multifractal nature of hippocampal neurons. Limiting dynamics to the soma compartment allows for ease of computation while retaining the necessary threshold dynamics for plausible spike activation. In addition, we employ our previous work on adaptive Nernst equilibria to account for variations in the average Nernst potential due to changes in intracellular and extra cellular ionic concentrations [MLS15].

The soma compartment for the reduced Traub model, presented by Pinsky and Rinzel, includes a leakage current, a sodium current with instantaneous activation (i.e. $m = m_\infty(V)$), and a delayed-rectifier potassium current [PR94].

$$C_{\mathrm{m}}\dot{V} = -\left(I_{\mathrm{Na}} + I_{\text{K-dr}} + I_{\mathrm{L}}\right) + I_{\mathrm{app}} \tag{3.2}$$

$$\dot{n} = \left(n_{\infty} - n\right)/\tau_n \tag{3.3}$$

$$\dot{h} = \left(h_{\infty} - h\right)/\tau_h \tag{3.4}$$

Where the ionic currents in Eq. 3.2 are

$$I_{\mathrm{Na}} = \bar{g}_{\mathrm{Na}} m_{\infty}^2 h \left(V - V_{\mathrm{Na}}\right) \tag{3.5}$$

$$I_{\text{K-dr}} = \bar{g}_{\text{K-dr}} n \left(V - V_{\mathrm{K}}\right) \tag{3.6}$$

$$I_{\mathrm{L}} = \bar{g}_{\mathrm{L}} \left(V - V_{\mathrm{L}}\right) \tag{3.7}$$

The forward and backward rate equations for n, h, and m are given in Table 4. The parameters used here are equivalent to those used by Traub et al. 1991, namely $\bar{g}_{\mathrm{L}} = 0.1$ μS, $\bar{g}_{\mathrm{Na}} = 30.0$ μS, $\bar{g}_{\text{K-dr}} = 25.0$ μS for CA1 neurons and $\bar{g}_{\text{K-dr}} = 15.0$ μS for CA3 neurons, $C_{\mathrm{m}} = 3$ $\mu\mathrm{F}/\mathrm{cm}^2$, $V_{\mathrm{L}} = 0$ mV, $V_{\mathrm{Na}} = 115$ mV, and $V_{\mathrm{K}} = -15$ mV. Eq. 3.2 may be written in a form common to all conductive-based models by introducing G_{eff} and V_{eq} (Eq. 3.8). Where G_{eff} and V_{eq} from Eq. 3.8 are given by Eqs. 3.9-3.10 for the reduced Traub model described above.

$$C_{\mathrm{m}}\dot{V} = -G_{\text{eff}} \left(V - V_{\text{eq}}\right) \tag{3.8}$$

$$G_{\text{eff}} = \left(\bar{g}_{\mathrm{Na}} m_{\infty}^2 h + \bar{g}_{\text{K-dr}} n + \bar{g}_{\mathrm{L}}\right) \tag{3.9}$$

$$V_{\text{eq}} = \left(\bar{g}_{\mathrm{Na}} m_{\infty}^2 h V_{\mathrm{Na}} + \bar{g}_{\text{K-dr}} n V_{\mathrm{K}} + \bar{g}_{\mathrm{L}} V_{\mathrm{L}}\right)/G_{\text{eff}} \tag{3.10}$$

The Hodgkin-Huxley (HH) model was originally designed under the assumption that the internal and external ionic concentrations act as charge reservoirs.

Table 4. The Rate Equations for the Reduced Miles-Traub Model. The forward (Alpha) and backward (Beta) rate equations used to craft the steady state and relaxation times for Eqs. 3.3-3.5.

	$\alpha(V)$	$\beta(V)$
n	$\frac{0.016\,(35.1-V)}{\exp\left(\frac{35.1-V}{5}\right)-1}$	$0.25\exp\left(\frac{20-V}{40}\right)$
h	$0.128\exp\left(\frac{17-V}{18}\right)$	$\frac{4}{1+\exp\left(\frac{40-V}{5}\right)}$
m	$\frac{0.32\,(13.1-V)}{\exp\left(\frac{13.1-V}{4}\right)-1}$	$\frac{0.28\,(V-40.1)}{\exp\left(\frac{V-40.1}{5}\right)-1}$

Therefore the amount of charge fluxing across the cellular membrane is miniscule compared to the total amount of charge stored either externally or internally. This assumption is quite valid for large diameter neurons. However, as we discuss further in Sec. 3.6, this assumption is less valid for hippocampal neurons. In this chapter we use a first-order reduction of the membrane equilibrium to account for the variations in the average Nernst potential. Eq. 3.11 shows this correction, the details of which are presented in Meier *et al.* 2015.

$$C_{\mathrm{m}}\dot{V} = (1-\zeta)\left[-G_{\mathrm{eff}}\left(V-V_{\mathrm{eq}}\right)\right] + I_{\mathrm{app}} \tag{3.11}$$

The feedback mechanism for shifting Nernst equilibrium, expanded to first order, is given by Eq. 3.12.

$$\zeta = \alpha\left(\frac{V_0 - V}{V - V_{\mathrm{eq}}}\right) \tag{3.12}$$

The total shift in the membrane equilibrium, in terms of the original membrane equilibrium V_{eq}, is given by Eq. 3.13.

$$\Delta V_{\text{eq}} = \frac{\alpha}{1-\alpha}\left(V_{\text{eq}} - V_0\right) \tag{3.13}$$

Fig. 23 shows the range of frequencies possible by selecting an (α, V_0) pairing within the HH conductive-based model presented above. This figure should be compared to Fig. 11 for the Morris-Lecar model.

One approach to modeling excitatory/inhibitory neurons in a network of neuron is to use the approach presented by Ermentrout *et al.* [EPG01], where excitatory neurons possess additional adaptation currents that are excluded from inhibitory neurons. Spike frequency adaptation due to charge depletion may be introduced via Eq. 3.14, where α is the same α used in Eq. 3.12.

$$\frac{d\alpha}{dt} = -\left(\alpha - \alpha_0\right)/\tau + \Delta\alpha \sum_{\text{spikes}} \delta\left(t - t_{\text{spike}}\right) \tag{3.14}$$

Fig. 24 shows the adaptation dynamics of Eq. 3.14. Fig. 25 shows the α dynamics in the 0.4mV slice of (V_0, α) space. As stated previously in this work, a single point in the (α, V_0) parameter space shifts the cellular equilibrium and this shift in equilibrium accounts for variations in ionic concentration.

It should be noted that network simulations are not used to derive the results of this chapter. However, the single-cell simulations performed here are relevant in the context of network dynamics and the experimental recordings which were used come straight from neurons operating within a bigger network.

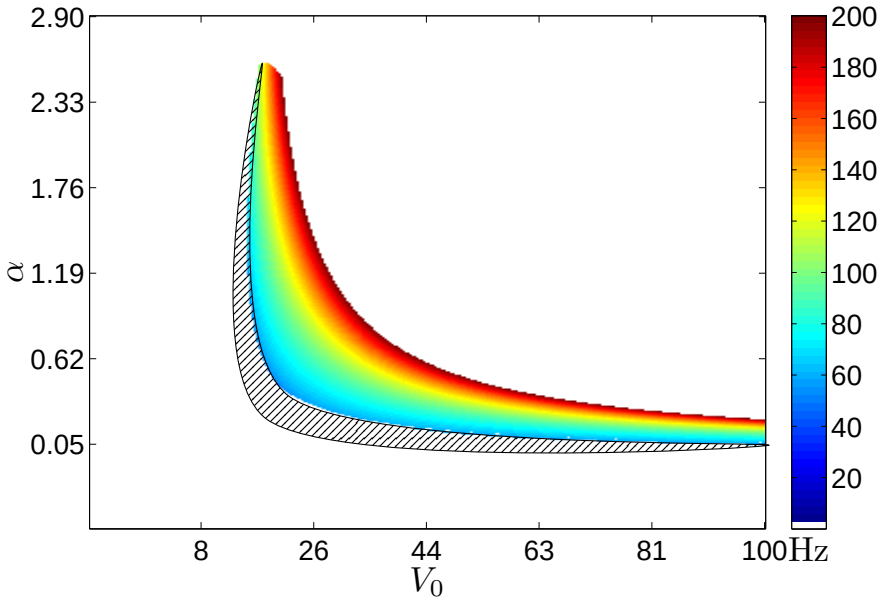

Figure 23. Plot of Alpha vs. V_0 Demonstrating the Wide Range of Frequencies these Parameters Provide. The color contrast indicates the natural frequency for a neuron with a particular (α, V_0) pairing. The shaded region indicates (α, V_0) values placed in the vicinity of a bifurcation event producing low frequency values.

The applied currents discussed in Sec. 3.3 are derived from *in vivo* recordings from Functional Cell Types (FTCs) in the CA1-CA3 rodent hippocampus, graciously provided by Fetterhoff *et al.* We consider these *ad hoc* applied currents to represent network inputs from a large number of neurons, some of which are streaming information directly into the cell. In Sec. 3.4 we demonstrate the ability to alter the correlation in ISIs for a single simulated cell receiving this derived *ad hoc* applied current.

The reduced Miles-Traub model is Class I excitable. Class I excitable cells produce arbitrarily low firing frequencies as a function of injected current. The modification introduced in Eq. 3.11 does not change this behavior. For the sections which follow, $|\alpha| < 1$ and $V_0 = 0.4$ mV. This ensures physiologically acceptable firing frequencies

while allowing a suitable resolution for transitions in multifractality to be observed. With these constraints we would like to call attention to the fact that $\alpha > 0$ corresponds to a depletion in intracellular charge and $\alpha < 0$ corresponds to an accumulation in intracellular charge. This follows directly from Eq. 3.13. All of this is relative to $\alpha = 0$, where the ionic concentration remains constant (typical HH dynamics). This allows us to easily relate the model parameter α to the variation in intracellular ionic concentration. This relationship is used in Sec. 3.3 and Sec. 3.4.

In Sec. 3.3 we describe our theoretical procedure. Our main goal was to investigate how the administration of various drugs could affect a single neuron's ability to process information. Our inclusion of variable Nernst potentials allowed for us to simulate varying degrees of ionic stress. By comparing multifractality at varying stress levels for each drug being considered we can compare a drug's effect relative to other drugs and relative to various doages of that drug.

3.3 Fitting Procedure for Deriving Applied Current from Experimental ISIs

In order to generate a function for the applied current that produces theoretical ISIs which match the experimental ISI values within a tolerance of less than one millisecond the following fitting procedure was employed. For an initial guess of the applied current function the procedure outlined in Fig. 26 was used. This procedure begins with a set of experimental ISI data. This set is then transformed from an instantaneous firing frequency to a step-wise applied current which occurs over the length of time necessary to produce the ISI signal.

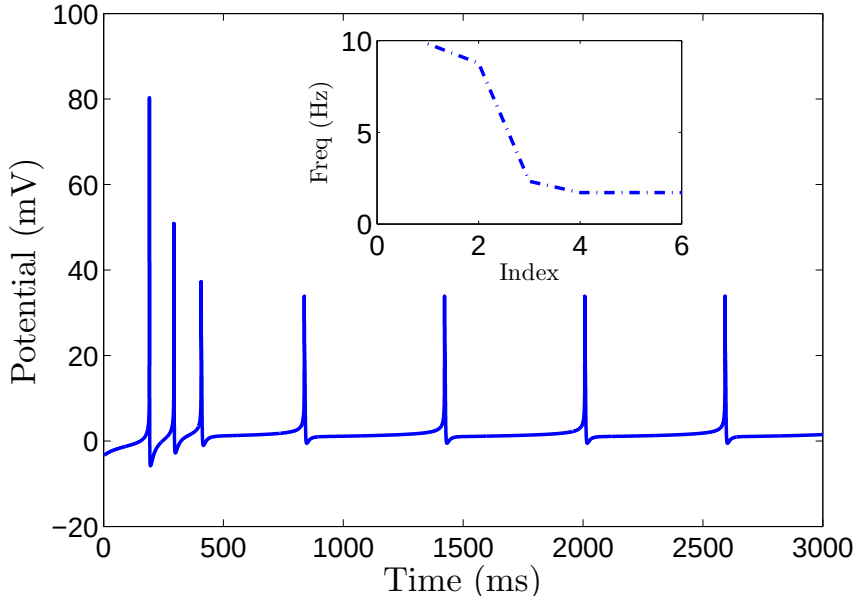

Figure 24. Spike Adaptation. Plot of spike adaptation after introducing a time-dependent equation for "α", Equation 3.14. Parameters were chosen such that the frequency range observed during adaptation was consistent with the known frequencies of Pyramidal neurons in the Hippocampus.

This produces an applied current function which assumes the ISI data is in its steady-state frequency. Therefore this is only a good initial guess for the applied current we are interested in.

Starting from this initial guess we consider each step in the applied current function individually. Fundamental to all Class I excitation neurons is the frequency vs. applied current relationship shown in Fig. 27. Knowing this allows for us to slightly vary the current value over each individual step in the step function until the firing frequency of the detailed Miles-Traub model matches the instantaneous firing frequency represented by the experimental ISI recordings.

For Class I excitable cells the relationship between the asymptotic frequency and applied current can be roughly approximated using Eq. 3.15.

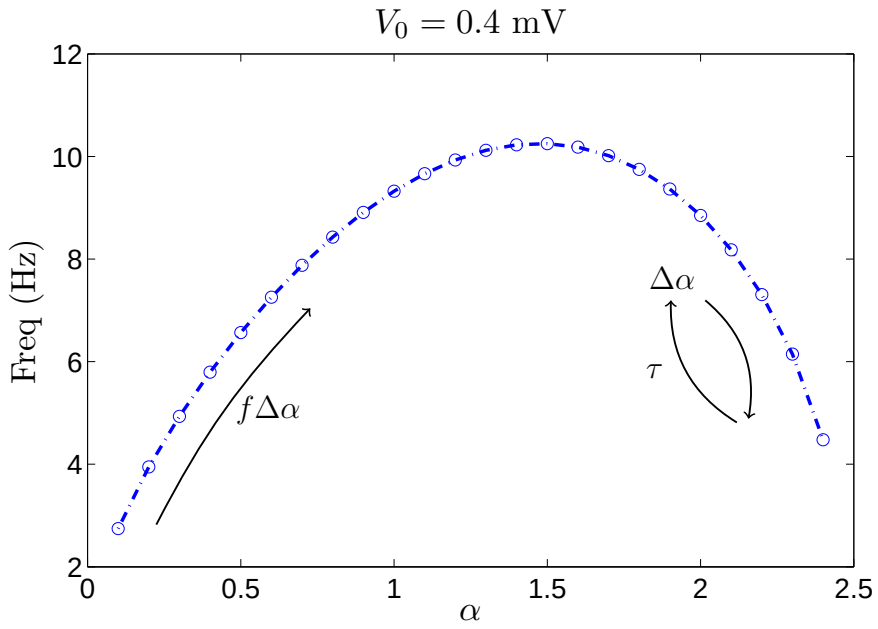

Figure 25. A Single Vertical Slice of the Alpha - V_0 Plane at V_0 Equals 0.4 mV, using the Reduced Miles-Traub Model. The initial jump in spiking frequency, which is typically associated with spike frequency adaptation currents, is produced here by the quadratic shape of the F-α curve. This parameter range was also used to generate Figure 24. Therefore both have a similar frequency range.

A representative fit is shown in Fig. 27.

$$f(I) = a\sqrt{(I-b)} + c \tag{3.15}$$

If a spike occurs at time t_i then the next spike, occurring at time t_{i+1}, may be approximated using Eq. 3.16 under the assumption that the instantaneous firing frequency is equivalent to the steady-state firing frequency at time t_i.

$$t_{i+1} = f(I(t_i))^{-1} + t_i \tag{3.16}$$

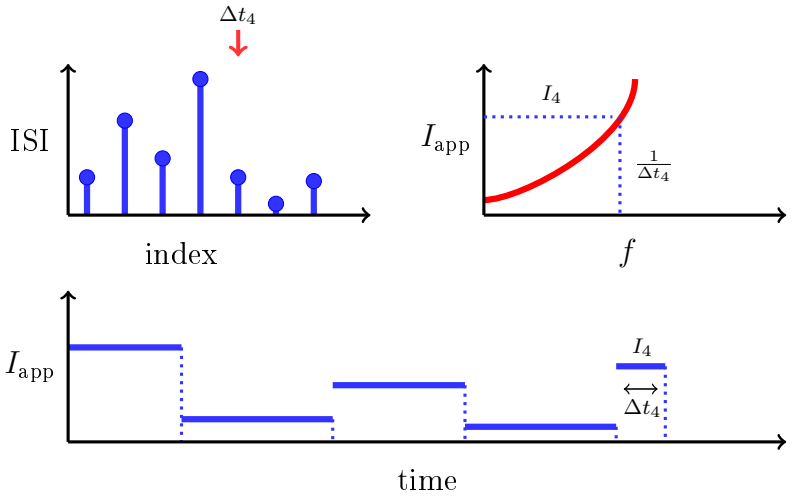

Figure 26. Minimization Procedure. The residuals between the experimental ISIs and theoretical steady-state ISIs were minimized by constructing an applied current which would produce nearly identical ISIs use the theoretical model.

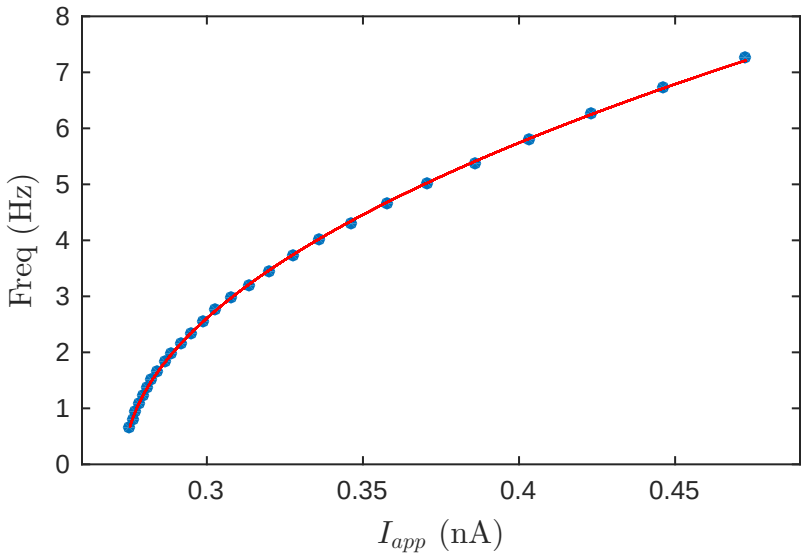

Figure 27. Plot of Asymptotic Frequency versus Applied Current. The blue points were computed using the reduced Miles-Traub model discussed in Sec. 3.2. The red line is a representative best-fit using Equation 3.15. Here $a = 16.24$, $b = 0.27$, and $c = -0.03$ for $\alpha = -0.2$ and $V_0 = 4$ mV.

The accuracy of this assumption depends on how quickly the cell achieves its steady-state firing frequency and how dramatically the applied current varies between two consecutive spiking events.

Eq. 3.16 is most accurate when the steady-state firing frequency occurs instantaneously and the applied current between two consecutive spiking events is held constant from t_i to t_{i+1}. However the results are quite robust, Fig. 28 shows a comparison between the ISIs generated using a reduced Miles-Traub model (discussed in Sec. 3.2) and those generated using Eq. 3.16 for the same applied current. In addition, the authors note that $f(I(t_i))dt$ works well as an inhomogeneous sampling rate for a stochastic cell modeled using a Poisson process. Poisson cells are commonly used to model network boundary conditions in order to simulate stochastic inputs from cortical projections [vVH01].

In this chapter we employ the approximate relationship between asymptotic frequency and applied current, Eq. 3.15, to generate a step-wise current function from ISIs measured in the CA3 region of the rodent hippocampus. In Fetterhoff *et al.* 2014 the authors made *in vivo* electrical recordings from the CA1-CA3 regions of the hippocampus of Long-Evans rats. Their analysis showed multifractality to be a better indicator than conventional methods for whether a particular neuron was involved in memory processing during a delayed nonmatch-to-sample task [FOS+14].

Provided with a set of N experimental ISI data points $\{\Delta t_0, ..., \Delta t_N\}$ between $t = t_0$ and $t = t_N$, a corresponding step-wise applied current function may be derived using Eq. 3.16.

Where each ISI, Δt_i, makes up a single current step, $I(t_i)$, which lasts from t_i to t_{i+1}.

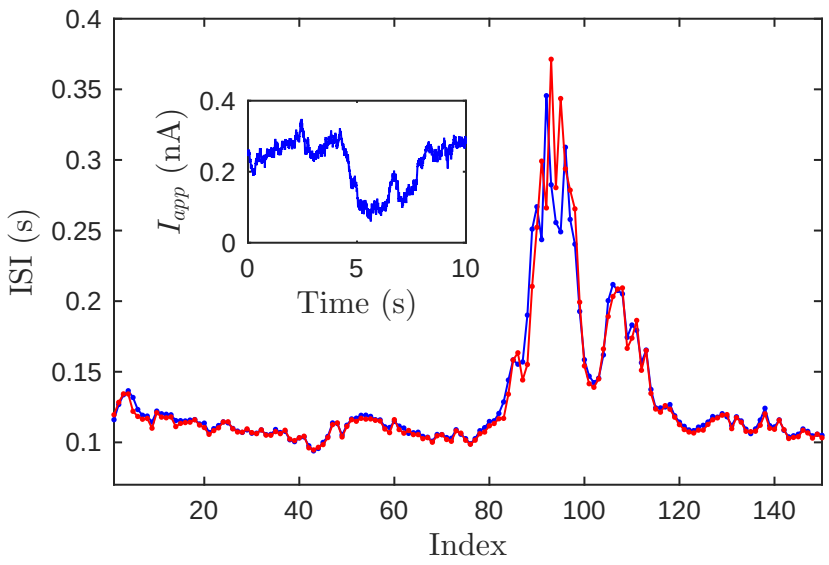

Figure 28. Comparison Between the ISIs for the Reduced Miles-Traub Model (blue) and Equation 3.16 (red). The inset plot is the applied current used to construct both the blue and red plots. The applied current is a simulated random walk normalized between 0.500 and 0.015 nA.

This provides us with a steady-state approximation for the applied current required to match the experimental ISIs. In Sec. 3.4 we derive a step-wise current function for each value of α explored. The reduced Miles-Traub model guarantees transient effects, which the approximate fit (Eq. 3.15) excludes. By observing the differences in multifractality for each parameter value tested and comparing these observations between experimental sets, we are able to probe fundamental differences between our experimental recordings.

3.4 Information Processing in the Hippocampus: Neurons Under the Influence of THC and CBD

Fig. 30 shows a comparison between experimental and theoretical ISIs. Using $\alpha = 0.15$ for the control and $\alpha = -0.15$ for THC we were able to achieve a percent

difference in the width of the singularity spectrum of 5.8% for control and 18.7% for THC. The density of ion channels is known to affect the firing class of the soma for neurons located in the hippocampus [ZBA10].

One possible reason for the less accurate comparison between the theoretical and experimental ISIs for THC is that the drug modifies the ion channel densities and changes the firing class by doing so. If this were the case then using a class I excitable model would introduce erroneous effects. A 4^{th}-order Runge-Kutta scheme with a $dt = 0.01$ ms was used to solve Eq. 3.2-3.4. Both the control and THC model cells were simulated long enough to acquire at least 2048 ISIs and these data were used to compare with the experimental recordings using multifractal analysis. The control cell was simulated for 260.43 s and for the THC cell simulations lasted 734.56 s. Each α value tested required calculating a new frequency versus applied current best-fit, as discussed in Sec. 3.3. The left-hand side of Table 5 shows the percent difference between the simulated and experimental ISIs using two different values of α. The right-hand side of Table 5 shows similar information but calculations where done relative to the THC recordings. The a, b, and c values for the best-fit (Eq. 3.15) which fit the corresponding values of α are also given in Table 5.

Functions for applied current were generated from experimental ISI data using the procedure described in Sec. 3.3. This procedure is outlined in Fig. 26. In varying ζ from Eq. 3.11, V_0 was set to 0.4 mV during all simulations.

This was done for two reasons: (1) a negative V_0 value would cause the net membrane current to hyperpolarize on the action potentials upstroke when α is negative (non-physical) and (2) lower values of V_0 allow for a wider range of α to be explored while keeping the membrane firing frequency within physiologically acceptable rates.

Table 5. Percent Difference in Singularity Spectra. This table shows how Alpha impacts the percent difference in the width of the singularity spectrum compared to the experimental data for both the control and THC administration. The a, b, and c values used to fit the asymptotic frequency to applied current, Eq. 3.15, are also listed.

	Control			THC		
α	0.15	0	-0.15	0.15	0	-0.15
$\Delta\%$	5.83%	15.02%	6.10%	21.05%	30.81%	18.75%
a	22.03	19.52	17.01	22.03	19.52	17.01
b	0.04	0.14	0.24	0.04	0.14	0.24
c	-0.89	-0.41	-0.10	-0.89	-0.41	-0.10

In fitting the theoretical model to the experimental ISIs, α was varied between -1 and 1 for all experimental recordings. A magnitude of 1 ensured that the current conductance, due to the depleted ionic charge, never reaches more than 100% of the net membrane conductance. For each parameter value tested, a corresponding I_{app} was derived using the method described in Sec. 3.3. The experimental data used to derive I_{app} was recorded from one neuron in one rat from the CA3 region of the hippocampus. We looked at the behavior of this neuron under the administration of Tetrahydrocannabinol (THC) and Cannabidiol (CBD). CBD was administered at dosages of 18 mg/kg and 15 mg/kg. The combination of THC plus CBD was administered at 2 mg/kg THC, 20 mg/kg CBD and 2 mg/kg THC, 25 mg/kg CBD. A control session followed each drug administrating session.

Fig. 29 shows the results. For each of the drug administrated sessions a series of computational experiments were conducted using our model. Each simulation assumes a slight shift in the intracellular ionic concentration. By compiling a number

of these simulations we theoretically explore how the multifractality of ISI data could have changed, given a shift in ionic concentration. In Fig. 29, the y-axis is the slope of the q^{th}-order Hurst exponent verses q. For whitenoise and monofractal signals this slope is zero. When the signal carries some multifractal nature this slope is greater than zero. The x-axis of Fig. 29 is our model parameter α. This parameter is used to vary the average ionic concentration for the cell.

Fig. 29 shows a definite transition in the multifractality of ISI data. This can be seen by the increase in the slope of H_q vs q (y-axis). All control recordings are indicated by black lines with white circle markers.

In addition, THC+CBD 2 mg/kg+25 mg/kg is cyan, THC+CBD 2 mg/kg+20 mg/kg is blue, CBD 18 mg/kg is green, and CBD 15 mg/kg is red. An earlier transition in the multifractality of ISI data for THC+CBD 2 mg/kg+25 mg/kg indicates a smaller shift in the ionic concentration is required to ascertain a multifractal signal. Due to the small diameter of hippocampal neurons, relative to most other neurons, the physiologically acceptable α value is slightly greater than zero. These curves suggest a general increase in multifractality with increasing charge depletion.

A positive value for α corresponds to a charge depleting current flowing opposite the direction of the net membrane current, whereas a negative value for α results in a depleting current which flows in the same direction as the membrane current.

Fig. 30 shows statistical data from a principle neuron within the CA1 region of the hippocampus. The same neuron both with THC administration and without was used to fit Eq. 3.12 for α using a stabilizing current of -0.37 nA and $V_0 = 4$ mV.

The stabilizing current and V_0 were set to achieve a physiologically plausible window for cellular frequency and applied current.

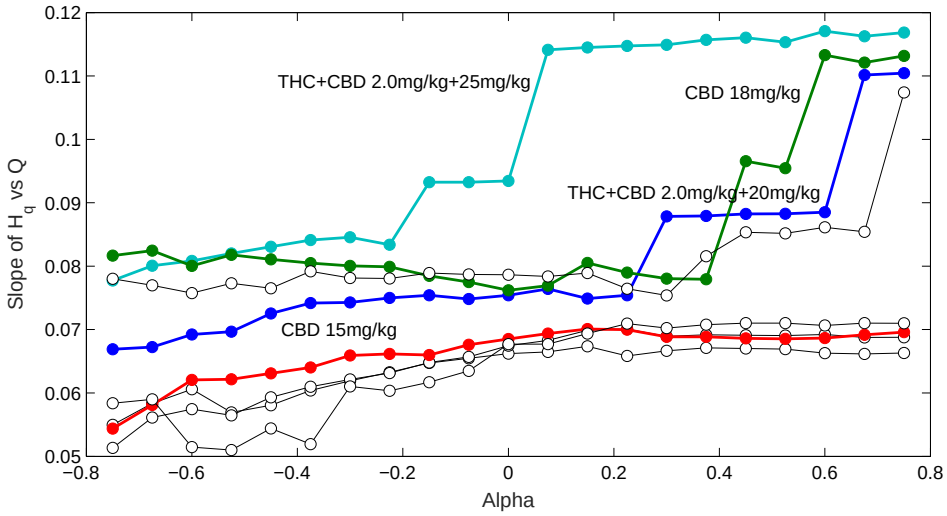

Figure 29. Alpha Shift for THC and CBD. The series of drugs presented in Section 3.4 were processed using our computational technique. The slope of H_q vs q is a measure of the multifractality of the signal. It can be seen that a transition exists in the degree of multifractality. This provides us with a quantitative measure for how various drugs influence the multifractality of a signal.

Fitting for α was done in order to have some quantifiable measure for the shift in feedback current due to the administration of THC. From Fig. 30:C we see a drop in α from 0.15 to 0.1265. Also, the median frequency varies dramatically between vehicle and THC. This can be explained due to a lack of variability in α. From Eq. 3.14 we know that spike frequency adaptation increases α resulting in increased firing frequencies. It is likely that the administration of THC decreases $\Delta\alpha$ which prevents spike frequency adaptation from occurring.

3.5 Discrete Networks Coupled via Dale's Principle

Before discussing the result of this chapter in the context of neuronal networks I would like to first discuss a generalized approach to modeling discrete networks.

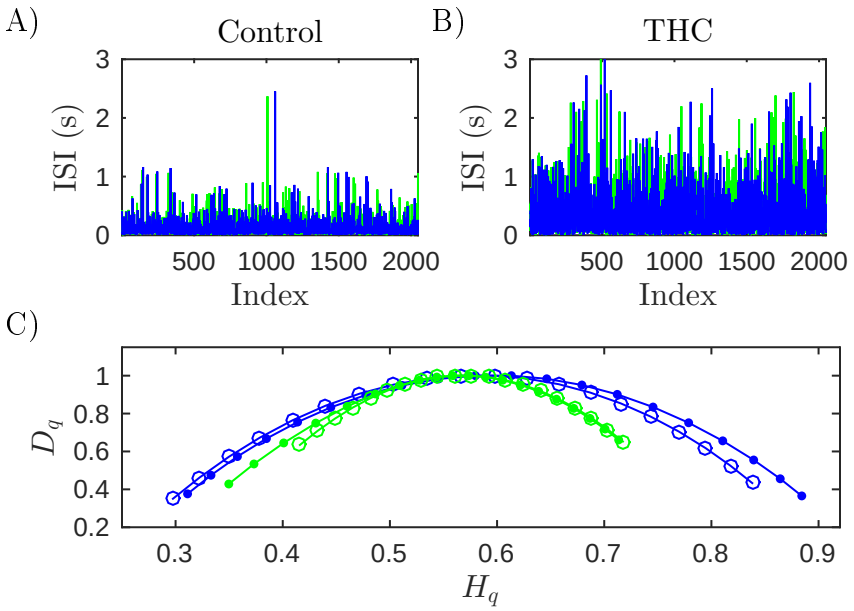

Figure 30. Comparison Between Experimental and Theoretical ISIs. Plots A and B show a comparison between experimental ISIs (green) and theoretical ISIs (blue) for the control (A) and THC (B) recordings. For the control $\alpha = 0.15$ and for THC $\alpha = -0.15$. Plot C shows the difference in the singularity spectra for both control (blue) and THC (green) for both experimental (hollow circles) and theoretical (filled circles) ISIs. The width of the singularity spectrum differs by 5.8% for the control and 18.7% for THC.

This discussion is relevant to potential future work which builds upon the results discovered here. Eq. 3.17 shows the diffusive coupling term for the i^{th} neuron in the network due to the j^{th} nearest neighbor.

$$I_{\text{syn}} = \sum_{i \neq j} D_{ij} \left(V_j - V_i \right) \tag{3.17}$$

The neuropercolative approach is useful for determining whether the i^{th} neuron produces excitatory post-synaptic pulses or inhibitory post-synaptic pulses governed by Dale's principle [HI97] (Eq. 3.18). In addition, this random selection process also de-

termines whether the i^{th} neuron includes the intrinsic adaptation current (Eq. 3.14), discussed previously. In accordance with Ermentrout et al. 2001, excitatory neurons possess the adaptation currents. These currents help approximate the calcium-dependent potassium currents which provide a high-threshold sharp spike-frequency adaptation to the cell.

$$\frac{\partial}{\partial V_j}\left(D_{ij}\left[V_j - V_i\right]\right) = \begin{cases} D_{ij} < 0 & \text{inhibitory} \\ D_{ij} \geq 0 & \text{excitatory} \end{cases} \tag{3.18}$$

The fraction of inhibitory neurons can be represented by the parameter "p".

Fig. 31 shows a typical percolation matrix with inhibitory neurons indicated as black squares and excitatory neurons as white squares. One further goal is to investigate how strongly the fraction of inhibitory neurons correlates with the spread of multifractality within the network. Experimental evidence shows 10-20% of the neurons within the hippocampus are inhibitory [CT12]. Perhaps multifractality is optimal within the range. Also, Fetterhoff et al. 2014 notes an increase in the fraction of inhibitory post-synaptic pulses following the administration of tetrahydrocannabinol (THC), which they show to decrease the fraction of multifractal neurons within the network. Therefore we hypothesize a decrease in multifractality as the fraction of inhibitory neuron increases past some optimal regime.

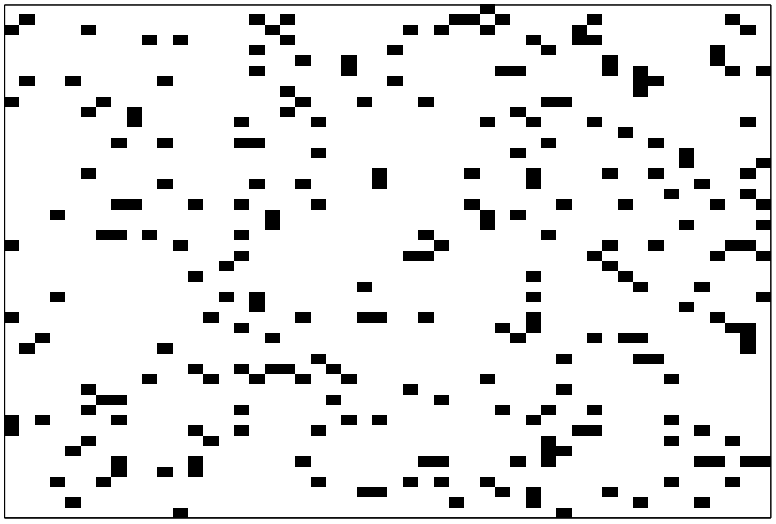

Figure 31. Percolation Approach to Neural Coupling. Plot of a typical percolation matrix ($p = 0.1$). The black squares represent inhibitory neurons within the network ($D_{ij} < 0$) and the white squares represent excitatory neurons ($D_{ij} \geq 0$). These matrices are generated randomly and provide an unbiased network structure from which to draw meaningful statistics.

3.6 Summary and Conclusion

In this chapter we investigate the relationship between Nernst variability, modeled as a first-order feedback current, and the multifractality of ISIs recorded in the CA3 region of the rodent hippocampus.

In Sec. 3.2 we present the reduced Miles-Traub model for modeling principle neurons within the CA1-CA3 regions of the hippocampus. In Sec. 3.3 we use approximate steady-state relationships to generate functions for applied current from experimentally recorded ISI data sets. In Sec. 3.4 we use these applied currents to investigate how Nernst variability can cause varying degrees of multifractality in neurons with differing dosages of THC and CBD.

Here we have made use of several new procedures and techniques. We have also employed our previous work on changing Nernst equilibria to allow for varying degrees of charge depletion to be modeled. As a baseline, the residuals between the steady-state ISIs for our theoretical model and the ISIs recorded experimentally were minimized. The results of this minimization provided us with a function for applied current which we then used to produce a set of ISI data using the detailed Miles-Traub model discussed in Sec. 3.2. By varying the charge depletion for each drug session we could then investigate the dependence between charge depletion and the information processing abilities for a neuron under the influence of a particular drug, or combination of drugs, at a particular dosage.

The assumption that ionic concentrations act as charge reservoirs is quite valid for the majority of neurons. Variations in ionic concentration may be brought about by a number of different mechanisms such as changes in cellular size [CUZ+09, MLS15]. In addition, the uptake of K^+ by glial cells will have an impact on the extracellular concentration of K^+, which would cause a shift in V_{eq}. The study of these effects may hold clinical applications for diseases such as epilepsy and tuberous sclerosis [Noo11]. If these diseases indeed have an appreciable effect on the cellular equilibrium, and thus the Nernst potential for individual ionic channels, then a simplified picture of the feedback mechanism is critical in understanding how these diseases may impact information processing.

Intracellular calcium dynamics have been shown to provide toggle and gain computations for Purkinje cells [For14]. This further suggests that changes in intracellular ionic concentration may have some impact of the capacity for neurons to process information. We provide a concrete theoretical framework for these variations and

demonstrate their effect on how neurons in the hippocampus process information. This provides a framework for further testing and establishes a new quantitative measure for how drugs impact the signal processing abilities of neurons. More testing will be needed to further solidify the validity and usefulness of this technique. THC alone has been shown to shorten the width of the multifractal spectrum [FOS+14]. Shortening of the width of the multifractal spectrum is associated with less multifractal signals. Our results suggest CBD has the potential to help block this effect.

The work presented here has important applications in neuronal network dynamics. The neuropercolative approach to network construction would allow for biological quantities, like charge depletion, to vary randomly across the network. The structure of dendritic branches and synaptic strengths both play an important role in how information propagates within a network made of neurons. Therefore, biological quantities which are known to affect the information processing abilities of single neurons could be varied across the network with ease. Such studies could produce a generalized understanding for how networks process information without being restricted to specific test cases.

One potential goal of future work is to investigate how strongly the fraction of inhibitory neurons correlates with the spread of multifractality within a network. The neuropercolative approach may be used to determine whether the i^{th} neuron in a network of neurons produces excitatory post-synaptic pulses or inhibitory post-synaptic pulses governed by Dale's principle [HI97] (Eq. 3.18).

Experimental evidence shows 10-20% of the neurons within the hippocampus are inhibitory [CT12]. Perhaps multifractality is optimal within the range. Also, Fetterhoff et al. 2014 notes an increase in the fraction of inhibitory post-synaptic pulses

following the administration of THC, which they show to decrease the fraction of multifractal neurons within the network. Therefore one hypothesis might be that multifractality decreases when the fraction of inhibitory neurons within a cortical network increases past some optimal regime.

Conservation of charge dictates that the variation in ionic concentration which we have considered for single neurons is inherently a network mechanism. The hippocampal region of the brain is very dense with neurons and this density is perhaps the necessary consequence of allowing ionic gradients to perform computations which take place over the course of multiple spiking events, where the ionic concentrations accumulate and dissipate in time.

CHAPTER IV

CONCLUSIONS AND FUTURE DIRECTIONS

This work provides a critical foundation for investigating variable Nernst potentials. A valid theoretical argument has been made for the inclusion of variable Nernst potentials in neurons with relatively small cellular diameters. These neurons are prevalent within information processing portions of the brain such as the hippocampus. Dynamics such as the soliton-like regime, discussed throughout Chp. II, provide new ways to think about the propagation of neural signals within the brain and should not be ignored when modeling signal propagation. These effects are relevant to both discrete and continuous networks of neurons.

Using the introductory content discussed in Chp. I, Chp. II employed the Andronov-Hopf bifurcation to a continuous network of neurons. The results demonstrated single-cell bursting as a result of communication between spatially separated neurons and a derivation of the soliton-like regime in the Fitzhugh-Nagumo model was presented. Fundamental to this work was the reduction made to the Hodgkin-Huxley like models to account for variable Nernst equilibria which result from variations in ionic concentration. Chp. III investigates the effect Nernst variability has on the multifractality of individual neurons. By varying the degree of charge depletion a phase transition was observed for the multifractality of single neurons. Remarkably, shifts in this phase transition were observed under the influence of different drugs at differing dosages. Such a result could prove useful as a sensitive measure for the effects drugs have on neurons within the brain.

In conclusion I would like to discussion the soliton-like regime in two spatial dimensions. In two dimensions we see spiral waves and intricate patterns begin to form. These patterns could provide a first look into memory as a means of spatiotemporal pattern formation. Fig. 32 is the result of simulating the following Fitzhugh-Nagumo system in the soliton-like regime.

$$\frac{1}{R}\left(\frac{\partial^2 V}{\partial x^2}+\frac{\partial^2 V}{\partial y^2}\right) = C\frac{\partial V}{\partial t}-\left(f(V+V_{\mathrm{eq}})-f(V_{\mathrm{eq}})\right)+N \tag{4.1}$$

$$\frac{\partial N}{\partial t} = \left(\sigma V - N\right)/\tau \tag{4.2}$$

Fitzhugh realized that Eq. 4.3 for $f(V)$ works well for approximating the generalized cubic-like nullcline of the Hodgkin-Huxley model [Fit61].

$$f(V) = -kV(V-V_{\mathrm{th}})(V-V_{\mathrm{A}}) \tag{4.3}$$

The parameters for this model are as follows: $R=1$, $C=1$, $k=8$, $V_{\mathrm{th}}=0.12$, $V_{\mathrm{A}}=1$, $\tau=1/0.05$, and $\sigma=8$. The soliton-like regime was first realized for the Fitzhugh-Nagumo system by changing τ to be a function of the trans-membrane potential (Eq. 4.4) [AM99].

$$\tau(V) = \left\{0.05+\Delta\epsilon\left(2-\tanh\left(\frac{V+0.04}{0.01}\right)+\tanh\left(\frac{V-0.75}{0.1}\right)\right)\right\}^{-1} \tag{4.4}$$

Where $\Delta\epsilon$ is a newly introduced parameter which is often set between 0.61 and 0.66. However, the system used to produce the spiral waves in Fig. 32 was derived using variable Nernst equilibria, Eq. 4.5, and not with $\tau(V)$, Eq. 4.4. Although, as discussed in Sec. 2.4 these two approaches are similar.

$$V'_{\mathrm{eq}} = V_{\mathrm{eq}} + \alpha\,(V_0 - V) \tag{4.5}$$

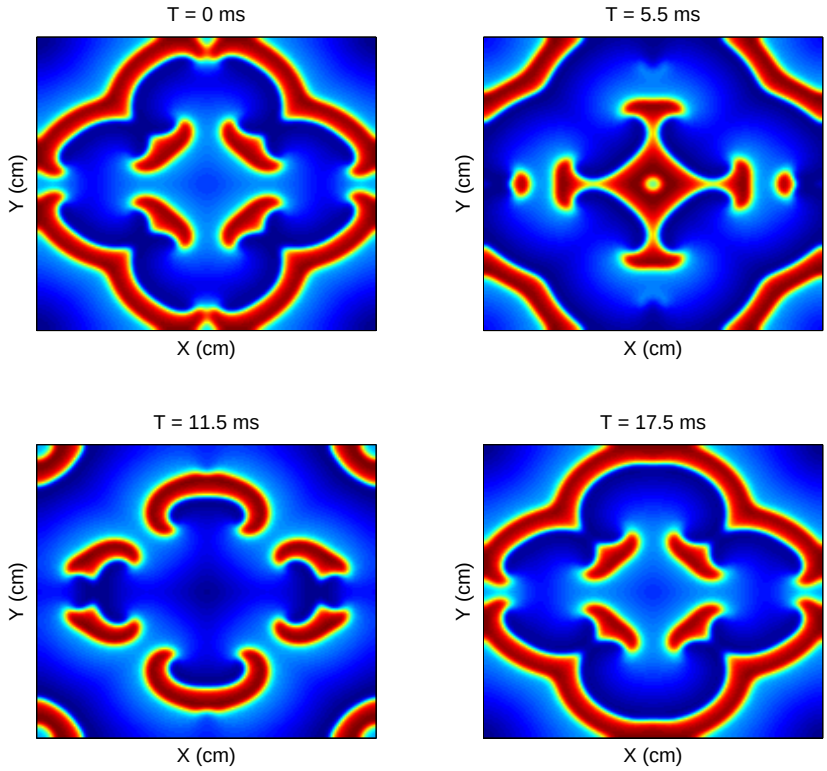

Figure 32. Two-Dimensional Reaction-Diffusion System. This figure shows four time slices for the Fitzhugh-Nagumo model of cellular excitation. These simulations were conducted within the soliton-like regime.

Where $\alpha\,(V_0 - V)$ is identical to V_δ from Eq. 2.27. For Fig. 32, $V_{\mathrm{eq}} = 0$, $\alpha = 0.1272$, and $V_0 = 0.5$. The alternating direction implicit method was used with $dt = 0.05$, and $dx = dy = 0.5$. No-flux boundaries were employed with x and y extending to 86 cm in both directions. The initial condition was a two spatial dimensional function of the trans-membrane potential and was acquired by running the simulation iteratively

over many intervals of time. The simulation eventually settled into this configuration. Simulating from this point results in a repeating pattern.

As shown in Chp. III, changes in model parameter α may cause variation in the multifractality of neural signals. Therefore, making the α parameter a function of position could allow for information processing to be investigated within continuous neuronal networks. Simulating higher spatial dimensions, along with quantifying the effects of drugs, make for two very promising directions for this work going forward.

REFERENCES

[ADAR91] David G. Amaral, Cynthia Dolorfo, and Pablo Alvarez-Royo, *Organization of ca1 projections to the subiculum: A pha-l analysis in the rat*, Churchill Livingstone Inc. **1** (1991), 415–435.

[AFR13] A. H. Abbasian, H. Fallah, and M. R. Razvan, *Symmetric bursting behaviors in the generalized fitzhughâĂŞnagumo model*, Biological Cybernetics (2013).

[AM97] O.V. Aslanidi and O.A. Mornev, *Can colliding nerve pulses be reflected?*, JETP Letters **65** (1997), 579–585.

[AM99] ———, *Soliton-like regimes and excitation pulse reflection (echo) in homogeneous cardiac purkinje fibers: Results of numerical simulations*, Journal of Biological Physics **25** (1999), 149–164.

[AMF+06a] Nikolai Axmacher, Florian Mormann, Guillen Fernández, Christian E. Elger, and Juergen Fell, *Memory formation by neural synchronization*, Brain Research Reviews **52** (2006), 170–182.

[AMF+06b] Nikolai Axmacher, Florian Mormann, Guillen Fernandez, Christian E. Elger, and Juergen Fell, *Memory formation by neuronal synchronization*, Brain Research Reviews **52** (2006), no. 1, 170–182.

[BC11] E. Barreto and J. R. Cressman, *Ion concentration dynamics as a mechanism for neuronal bursting*, Journal of Biological Physics **37** (2011), 361–373.

[BV91] Albert Barabasi and Tamas Vicsek, *Multifractality of self-affine fractals*, Physical Review A **44** (1991), 2730–2733.

[BW01] S. Marc Breedlove and Neil V. Watson, *Biological psychology: An introduction to behavioral, cognitive, and clinical neuroscience, seventh edition*, Wadsworth Publishing, 2001.

[CGAO98] S. Commins, J. Gigg, M. Anderson, and SM. O'Mara, *The projection from hippocampal ca1 to the subiculum sustains long-term potentiation*, Neuroreport **9** (1998), 847–50.

[CT12] Simon Chamberland and Lisa Topolnik, *Inhibitory control of hippocampal inhibitory neurons*, Frontiers in Neuroscience **6** (2012).

[CUZ+09] J.R. Cressman, G. Ullah, J. Ziburkus, S.J. Schiff, and E. Barreto, *The influence of sodium and potassium dynamics on excitability, seizures, and the stability of persistent states: I. single neuron dynamics*, Journal of Computational Neuroscience (2009).

[DCB+11] Dominique Debanne, Emilie Campanac, Andrzej Bialowas, Edmond Carlier, and GisÃÍle Alcaraz, *Axon physiology*, American Physiological Society **91** (2011), 555–602.

[DZ11] Lixia Duan and Dehong Zhai, *Bifurcation and bursting in morris-lecar model for class i and ii excitability*, Discrete and Continuous Dynamical Systems (2011).

[EC04] Howard Eichenbaum and Neal J. Cohen, *From conditioning to conscious recollection: Memory systems for the brain*, Oxford University Press, 2004.

[EPG01] Bard Ermentrout, Matthew Pascal, and Boris Gutkin, *The effects of spike frequency adaptation and negative feedback on the synchronization of neural oscillators*, Neural Computation **13** (2001), 1285–1310.

[Erm96] Bard Ermentrout, *Type 1 membranes, phase resetting curves, and synchrony*, Neural Computation **8** (1996), 979–1001.

[Fit61] Richard Fitzhugh, *Impulses and physiological states in theoretical models of nerve membrane*, Biophysical Journal **1** (1961), 445–466.

[For13] M. D. Forrest, *Mathematical model of bursting in dissociated purkinje neurons*, PLoS ONE **8** (2013), e68765.

[For14] ———, *Intracellular calcium dynamics permit a purkinje neuron model to perform toggle and gain computations upon its inputs*, Frontiers in Computational Neuroscience **8** (2014), 86.

[FOS+14] Dustin Fetterhoff, Ioan Opris, Sean L. Simpson, Sam A. Deadwyler, Robert E. Hampson, and Robert A. Kraft, *Multifractal analysis of information processing in hippocampal neural ensembles during working memory under thc administration*, Journal of Neuroscience Methods **1** (2014), 1–18.

[GdADM10] A. V. Goltsev, F. V. de Abreu, S. N. Dorogovtsev, and J. F. F. Mendes, *Stochastic cellular automata model of neural networks*, Physical Review E **81** (2010), no. 6, 061921.

[GPBM+14] Alfredo Gonzalez-Perez, Rima Budvytyte, Lars D. Mosgaard, SÃÿren Nissen, and Thomas Heimburg, *Penetration of action potentials during collision in the median and lateral giant axons of inverebrates*, Physical Review X **4** (2014), 031047.

[HH52] A. L. Hodgkin and A. F. Huxley, *A quantitative description of membrane current and its application to conduction and excitation in nerve*, Journal of Physiology **117** (1952), 500–544.

[HI97] Frank Hoppensteadt and Eugene Izhikevich, *Weakly connected neural networks*, Springer **126** (1997), 13–16.

[Hod48] Alan Hodgkin, *The local electric changes associated with repetitive action in a non-medullated axon*, Journal of Physiology **107** (1948), 165–181.

[HWM91] RM Harris-Warrick and E. Marder, *Modulation of neural networks for behavior*, Annual Review of Neuroscience **14** (1991), 39–57.

[IBH05] Enno de Lange Igor Belykh and Martin Hasler, *Synchronization of bursting neurons: What matters in the network topology*, Physical Review Letters **94** (2005), no. 18, 188101.

[Ihl12] Espen A. F. Ihlen, *Introduction to multifractal detrended fluctuation analysis in matlab*, Frontiers in Physiology **3** (2012), 1–18.

[Izh04] Eugene M. Izhikevich, *Which model to use for cortical spiking neurons?*, Institute of Electrical and Electronics Engineers **15** (2004), 1063–1070.

[Izh10] ———, *Dynamical systems in neuroscience: The geometry of excitability and bursting*, The MIT Press, One Rogers Street Cambridge MA 02142-1209, 2010.

[KK73] V. I. Krinskii and Yu. M. Kokoz, *Analysis of equations of excitable membranes - i. reduction of the hodgkin-huxley equations to a second order system.*, Biofizika **18** (1973), 506–511.

[KS09] James Keener and James Sneyd, *Mathematical physiology*, Springer, 233 Spring Street New York, NY 10013-1578, 2009.

[LEL75] Harold Lecar, Gerald Ehrenstein, and Ramon Latorre, *Mechanism for channel gating in excitable bilayers*, Annals New York Academy of Sciences **264** (1975), 304–313.

[LYL+12] Xiao-Yu Lin, Jing Yang, Hui-Ming Li, San-Jue Hu, and Jun-Ling Xing, *Dorsal root ganglion compression as an animal model of sciatica and low back pain*, Neuroscience Bulletin **5** (2012), 1–13.

[M.74] Milner Peter M., *A model for visual shape recognition.*, Psychological review **81** (1974), no. 6, 521–535.

[MB01] E. Marder and D. Bucher, *Central pattern generators and the control of rhythmic movements*, Current Biology **11** (2001), no. 23, 986–996.

[ML81] C. Morris and H. Lecar, *Voltage oscillations in the barnacle giant muscle fiber*, Journal of Biophysics **35** (1981), 193–213.

[MLS15] Stephen R. Meier, Jarrett L. Lancaster, and Joseph M. Starobin, *Bursting regimes in a reaction-diffusion system with action potential-dependent equilibrium*, PLOS ONE **10** (2015), e0122401.

[NC13] Wilten Nicola and Sue Ann Campbell, *Bifurcations of large networks of two-dimensional integrate and fire neurons*, Journal of computational neuroscience **35** (2013), 87–108.

[NHCG98] Christopher A. Del Negro, Chie-Fand Hsiao, Scott H. Chandler, and Alan Garfinkel, *Evidence for a novel bursting mechanism in rodent trigeminal neurons*, Biophysical Journal **75** (1998).

[Noo11] H. Noori, *The impact of the glial spatial buffering on the k+ nernst potential*, Cognitive Neurodynamics **5** (2011), 285–291.

[O'M05] Shane O'Mara, *The subiculum: what it does, what it might do, and what neuroanatomy has yet to tell us*, Journal of Anatomy **207** (2005), 271–282.

[oS64] National Bureau of Standards, *Handbook of mathematical functions*, Dover, 1964.

[PB07] Robert Plonsey and Roger C. Barr, *Bioelectricity: A quantitative approach*, Springer, 233 Spring Street New York, NY 10013-1578, 2007.

[PR94] Paul F. Pinsky and John Rinzel, *Intrinsic and network rhythmogenesis in a reduced traub model for ca3 neurons*, Journal of Computational Neuroscience **1** (1994), 39–60.

[QR04] Bo Qian and Khaled Rasheed, *Hurst exponent and financial market predictability*, IASTED Conference on Financial Engineering and Applications (2004), 203–204.

[RE89] John Rinzel and Bard Ermentrout, *Methods in neuronal modelling: From synapses to networks*, MIT Press (1989).

[RFT+08] Enrico Rossoni, Jianfeng Feng, Brunello Tirozzi, David Brown, Gareth Leng, and Francoise Moos, *Emergent synchronous bursting of oxytocin neuronal network*, PLoS one **4** (2008), 1–12.

[RGWB69] Harald Reuter and Jr. George W. Beeler, *Calcium current and activation of contraction in ventricular myocardial fibers*, Science **163** (1969), no. 3865, 399–401.

[RKM98] N. G. Rambidi, T. O.-O. Kuular, and E. E. Makhaeva, *Information-processing capabilities of chemical reaction-diffusion systems. 1. belousov-zhabotinsky media in hydrogel matrices and on solid supports*, Advanced Materials For Optics And Electronics **8** (1998), 163–171.

[SJT+00] NP Staff, HY Jung, T Thiagarajan, M Yao, and N Spruston, *Resting and active properties of pyramidal neurons in subiculum and ca1 of rat hippocampus*, Journal of Neurophysiology **84** (2000), 2398–408.

[SKM94] Frances K. Skinner, Nancy Kopell, and Eve Marder, *Mechanisms for oscillation and frequency control in reciprocally inhibitory model neural networks*, Journal of Computational Neurosience **1** (1994), no. 1, 69–87.

[SL13] Tilo Schwalger and Benjamin Lindner, *Patterns of interval correlations in neural oscillators with adaptation*, Frontiers in Computational Neuroscience **7** (2013).

[Sla08] Angela Slavova, *Reaction-diffusion cellular neural network models*, 9th WSEAS International Conference on Neural Networks (2008).

[SM57] William Scoville and Brenda Milner, *Loss of recent memory after bilateral hippocampal lesions*, Journal of Neurology Neurosurgery and Psychiatry **20** (1957), 11–21.

[Tre93] Alessandro Treves, *Mean-field analysis of neuronal spike dynamics*, Biophysic **4** (1993), 259–284.

[TWMM91] Roger D. Traub, Robert K. S. Wong, Richard Miles, and Hillary Michelson, *A model of a ca3 hippocampal pyramidal neuron incorporating voltage-clamp data on intrinsic conductances*, Journal of Neurophysiology **66** (1991), 635–650.

[UJBS09] Ghanim Ullah, John R. Cressman Jr., Ernest Barreto, and Steven J. Schiff, *The influence of sodium and potassium dynamics on excitability, seizures, and the stability of persistent states: Ii. network and glial dynamics*, Journal of Computational Neurosience **26** (2009), no. 2, 171–183.

[vVH01] C. van Vreeswijk and D. Hansel, *Patterns of synchrony in neural networks and spike adaptation*, Neural Computational **5** (2001), 959–992.

[WG90] MP Witter and HJ Groenewegen, *The subiculum: cytoarchitectonically a simple structure, but hodologically complex*, Progress in brain research **83** (1990), 47–58.

[WH88] Robert Williams and Karl Herrup, *The control of neuron number*, Annual Review Neuroscience **11** (1988), 423–453.

[WLL+12] Yu Wu, Wenlian Lu, Wei Lin, Gareth Leng, and Jianfeng Feng, *Bifurcations of emergent bursting in a neuronal network*, PLoS one **7** (2012), 1–12.

[ZBA10] Hugo Zeberg, Clas Blomberg, and Peter Arhem, *Ion channel density regulates switches between regular and fast spiking in soma but not in axons*, PLoS Computational Biology **6** (2010).